

Bidirectional wide range and high voltage gain buck-boost DC-DC converter for EV chargers empowering V2G-G2V applications

Zahra Gholami¹  | Rahim Ildarabadi¹  | Hamed Heydari-Doostabad² |
 Mohammad Monfared³  | Terence O'Donnell²

¹Department of Electrical Engineering, Hakim Sabzevari University, Sabzevar, Iran

²School of Electrical and Electronic Engineering, University College Dublin, Dublin, Ireland

³Faculty of Science and Engineering, Swansea University, Swansea, U.K.

Correspondence

Rahim Ildarabadi, Department of Electrical Engineering, Hakim Sabzevari University, Sabzevar, Iran.
 Email: r.ildar@hsu.ac.ir

Funding information

Science Foundation Ireland, Grant/Award Number: SFI/21/SPP/3756

Abstract

This paper proposes a new wide range bidirectional buck-boost dc-dc converter with improved voltage gain in either forward (discharging) or backward (charging) direction for electric vehicle (EV) applications. The converter has high-voltage gain ratio with no theoretical limits in the output voltage in both directions, and presents a good balance between the component count, number of conducting components, semiconductor device ratings, having direct connection between input and output terminals, and efficiency which makes it a practical solution for the EV charger levels 1, 2, and 3 power converter unit. The operating principle, steady-state characteristics including the current and voltage stress of the switches, and comparison with other state of the art dc-dc bidirectional converters are explained in detail. In order to validate the theoretical analysis, a 500 W, 200 V or 40 V to 180 V laboratory prototype is implemented. The obtained results confirm the applicability of this structure and demonstrate a peak efficiency of 97.2% in the forward and 97.6% in the backward direction modes of operation.

1 | INTRODUCTION

Electrification of transport coupled with increased generation from renewables is a central pillar in the strategy to decarbonize the energy system. Electric Vehicle (EV) charging, however, places a very significant extra burden on the electricity demand so that power conversion efficiency in the charging process is critically important. On the other hand it is recognized that the energy storage capacity of EV batteries could provide a significant resource to aid with renewable integration, which leads to the concept of Vehicle to Grid [1, 2].

In a V2G implementation, as illustrated in Figure 1, the bidirectional power electronic converters act as an interface hardware stage between the electric vehicle supply equipment (EVSE) and the battery storage pack. This means that bidirectional converters should offer vehicle to grid (V2G) and grid to vehicle (G2V) services at high energy transfer efficiency, wide output voltage range, limitless voltage gain ratio, low cost, and high performance [3–5]. A typical V2G scenario would involve charging the EV battery from the grid during periods of low

energy demand (e.g. nighttime) or high renewable generation, then supplying the stored energy back to the grid for example to reduce frequency fluctuations [6] or reduce utility costs during peak usage [7].

A buck-boost wide range gain bidirectional dc-dc converter is required to adapt the voltage levels of the battery (V_b) and the grid side converter dc-link voltage ($V_{dc-link}$) since the battery voltage varies [8].

Conventional bidirectional boost/buck converters have been widely adopted by researchers due to their simple structures [9–11]. However, the conventional buck/boost converters have relatively low voltage gain ratios. Higher voltage gain ratio converters have the advantage that they can achieve the voltage gain at lower and less extreme value of duty cycle, which can in turn reduce switch voltage and current stresses and lower losses. In addition, the boost/buck converters have a limitation in that they can transfer power in only one mode i.e. boost or buck. Therefore, the bidirectional buck-boost converters with step-down and step-up voltage gain ratio i.e. $D/(1-D)$ have been adopted to regulate the battery and the dc-link voltages. Hence,

This is an open access article under the terms of the [Creative Commons Attribution-NonCommercial-NoDerivs](https://creativecommons.org/licenses/by-nc-nd/4.0/) License, which permits use and distribution in any medium, provided the original work is properly cited, the use is non-commercial and no modifications or adaptations are made.

© 2023 The Authors. *IET Power Electronics* published by John Wiley & Sons Ltd on behalf of The Institution of Engineering and Technology.

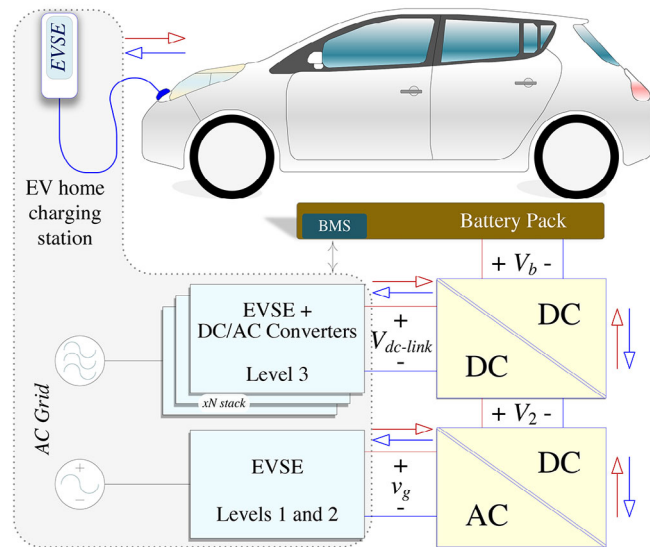


FIGURE 1 Electric vehicle on-board chargers and charging station.

these converters can regulate the battery and the dc-link voltages under a wider range of the source variations, and have become more popular.

The presented bidirectional buck-boost dc-dc converter in [12] transfers stored energy between the battery and the dc-link with a low voltage gain with the potential for shoot through (ST) issues which should be reduced by use of a dead-time.

Although the half-bridge bidirectional buck-boost dc-dc converter in [13] has no ST problem at the input and output sides, its voltage gain ratio is low.

Switched capacitor converters can attain high voltage gains. The capacitors store and release the energy during every switching period. The pivotal benefits of this type of converter are, simple structure, high voltage gain, high power density, high efficiency, light weight, low cost, and better integration capability because of the absence of inductors [14–17]. However, this type of converter is inactive for certain voltage gain ranges, for example the converter in [17] is inactive for the voltage gain between $1/3$ to 3 . Furthermore, the use of large capacitors demand a significant amount of charging current which impacts the rating and losses of active components of a circuit. Moreover, the improved suitability for integration is only useful at very low powers-switched where on-chip integration of capacitors is easier than inductors.

The hybrid converter which is a combination of switched capacitor and inductor based converter, has been introduced to solve the drawbacks of the switched capacitor converters by adding an inductor.

In this regard and to improve the voltage gain ratio of the conventional bidirectional buck-boost dc-dc converter in both directions, converters in [18, 19] presented higher and wider voltage gain ratios for both forward and backward directions than the conventional buck-boost converter. However, the lack of direct connection between input and output terminals gives rise to EMI noise issues and still further improvements in the voltage gain ratio would be beneficial.

The converters presented in [20–22] are able to provide a wide quadratic voltage gain ratio i.e. $D^2/(1-D)^2$ for both forward and backward directions. With a quadratic voltage gain ratio, the bidirectional converter in [23] suffers from low semiconductor utilization. The quadratic converters solve ST and limits with the voltage gain, but they are complex due to their high component count.

In many studies, the voltage gain of the conventional boost/buck dc-dc converter is improved such as [15, 16, 24, and 25] in exchange for extra cost, complexity, and losses. Furthermore, the voltage gain range of the converter in [15] is from 0 to 0.25 in step-down and from 4 to ∞ in step-up. For the converters in [15 and 16] the range is from 0 to 0.5 and from 2 to ∞ . Therefore, these converters do not function for the voltage gain range between 0.25 to 4 and 0.5 to 2 , respectively. Moreover, similar to the conventional boost/buck converter, the converters in [15, 16, 24, and 25] have the limitation that they transferring energy only in one mode either buck or boost.

In this paper, in order to obtain high buck-boost voltage gain with a wider output voltage range a new bidirectional dc-dc converter is proposed. Unlike some of the previous converters, the proposed converter offers high voltage gain ratio which is active between 0 and ∞ for the output voltage in both directions. Furthermore, the current controller is adapted for indirect battery current control, which offers accurate, fast, and smooth operation under different states of charge (SoC). The direct electrical connection between input and output terminals is preserved which can significantly reduce the EMI noise. Finally, the proposed dc-dc converter is adopted as the front stage for a grid-connected full-bridge dc-ac converter.

The rest of this paper is organized as follows. The proposed bidirectional dc-dc converter is presented in section 2. Section 3 is devoted to the practical considerations and design calculations for the proposed converter. A comprehensive comparison to the previous state of art converters is presented in section 4, the proposed dead-beat controller description is given in section 5 and the experimental verification is provided in section 6. Finally, section 7 concludes the paper.

2 | DC-DC STAGE OF PROPOSED EV CHARGER OPERATION PRINCIPLE

Figure 2 shows the proposed bidirectional EV charger converter structure. V_b and L_b denote the battery side voltage and battery current filter, respectively. The dc-dc stage of the proposed EV charger consists of four switches S_1 , S_2 , S_3 , and S_4 , two inductors L_1 and L_2 and three capacitors C_1 , C_2 , and C_3 . V_1 and V_2 denote the primary and the secondary side voltages, respectively. The conventional full-bridge converter consists of four switches S_A , S_B , S_C , and S_D , with inductance filter L_g is used to connect the proposed dc-ac stage to the ac grid.

Figure 3 shows the forward (discharging) and the backward (charging) operations in continuous conduction mode (CCM) and discontinuous conduction mode (DCM), and follows the detailed analysis.

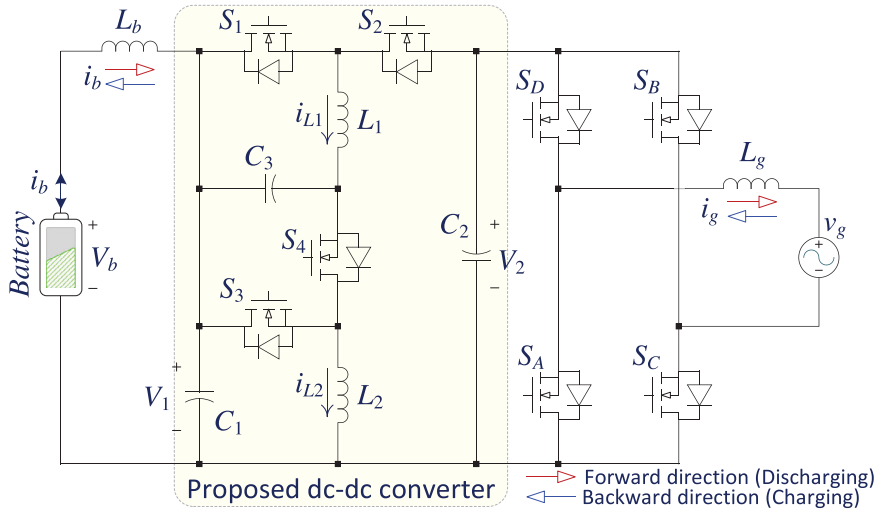


FIGURE 2 Proposed EV home charger, dc-dc and dc-ac converters.

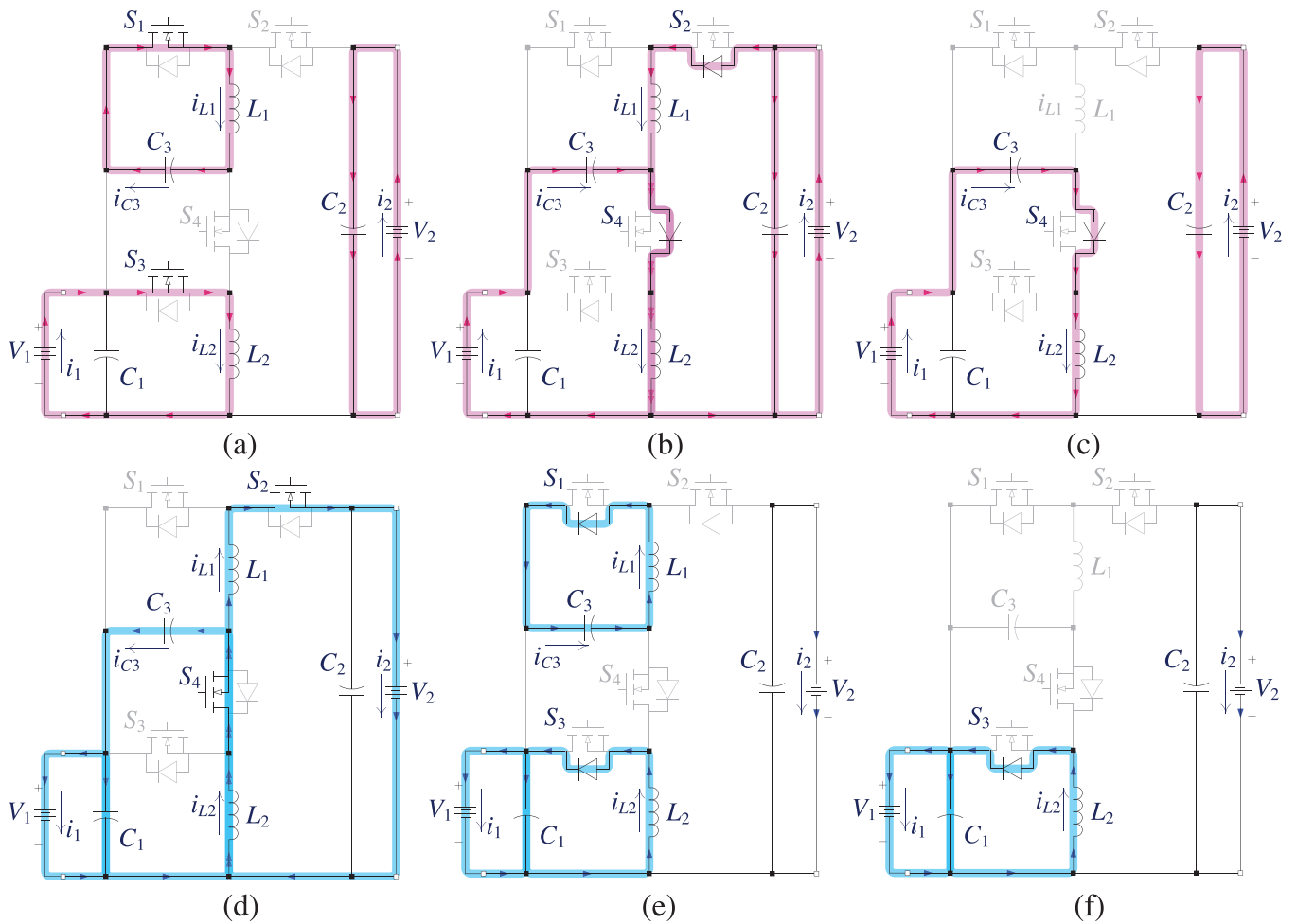


FIGURE 3 Equivalent circuit of the proposed converter in forward mode (a) state 1, (b) state 2, (c) state 3 and backward mode (d) state 1, (e) state 2, (f) state 3.

2.1 | Forward direction operation mode

In the forward direction operation or the discharging mode, the power flows from V_1 to V_2 . There are two states of operation

associated with CCM and four states associated with DCM operation as defined in the following.

State 1 of CCM and DCM $[0-t_1]$: During $0 \leq t < DT_s$ or the state-1 of the forward direction mode and according to

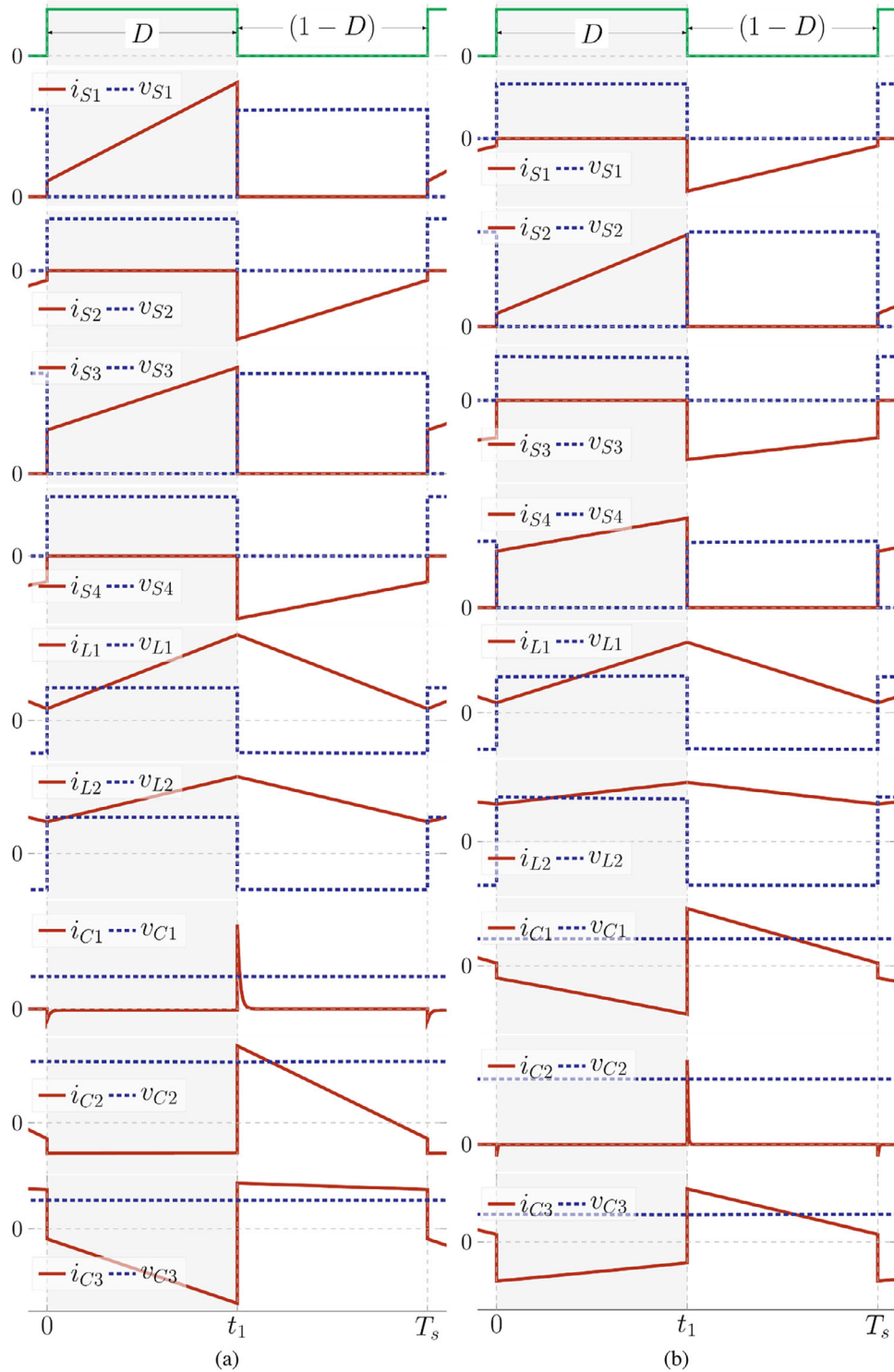


FIGURE 4 Typical waveforms of CCM: (a) forward and (b) backward modes.

Figure 3(a), S_1 and S_3 are turned on, while S_2 and S_4 are turned off. In this state, L_2 is charged by the input dc source. Thus, the current through L_2 increases, whereas the energy of L_1 is increased by the released energy from C_3 . According to the typical time-domain waveforms in Figure 4(a), the derived current and voltage equations are as follows:

$$\begin{cases} v_{L1} = L \frac{dl_1}{dt} = v_{C3} \\ v_{L2} = L \frac{dl_2}{dt} = V_1 \\ i_{C3} = C_3 \frac{dv_{C3}}{dt} = -i_{L1} \end{cases} \quad (1)$$

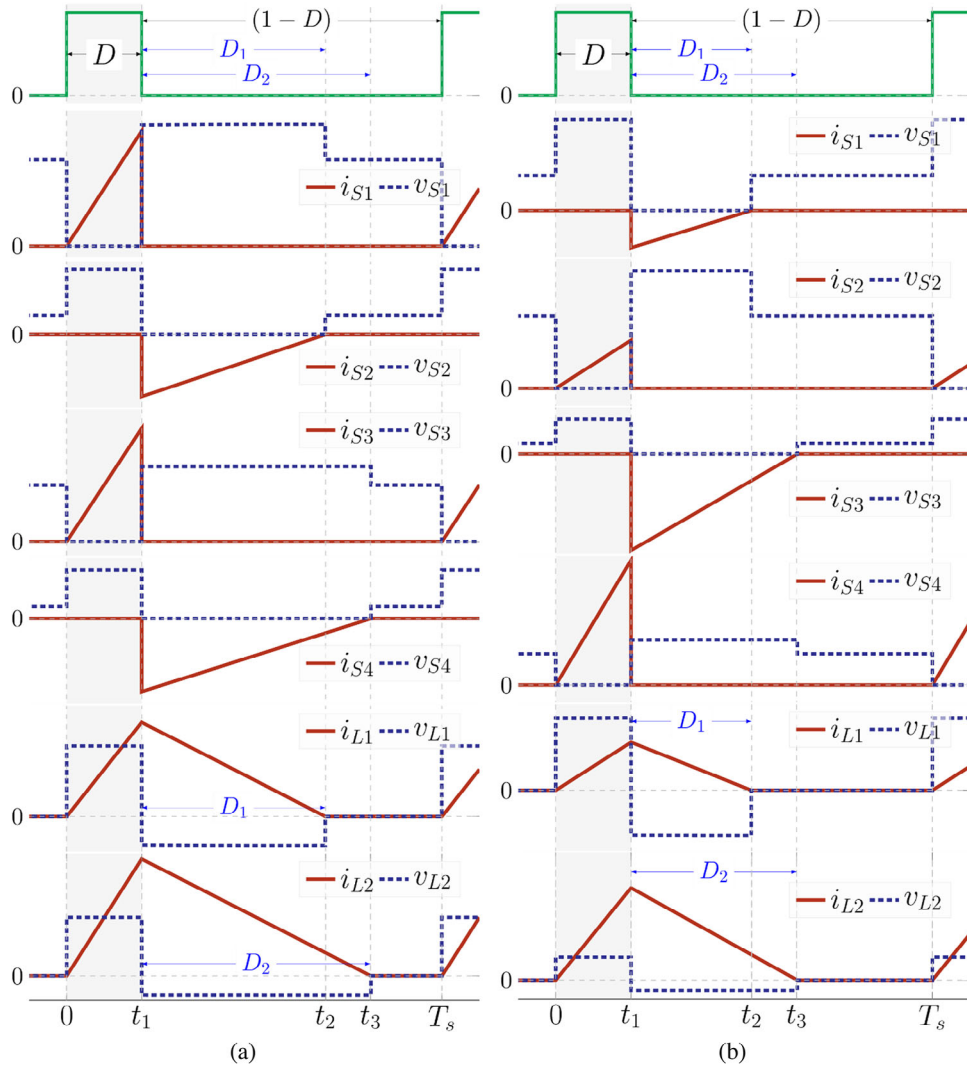


FIGURE 5 Typical waveforms of DCM: (a) forward and (b) backward modes.

State 2 of CCM $[t_1-T_s]$ and DCM $[t_1-t_2]$: Contrary to state 1, during this interval, as shown in Figure 3(b), S_1 and S_3 are turned off whereas the body diodes of S_2 and S_4 are conducting. The inductor L_1 releases its energy into the secondary side through the body diode of S_2 . Similarly, L_2 and the primary side source release energy into C_3 through the body diode of S_4 . Therefore, we have:

$$\begin{cases} v_{L1} = L \frac{dL_1}{dt} = -V_2 - V_1 + v_{C3} \\ v_{L2} = L \frac{dL_2}{dt} = V_1 - v_{C3} \\ i_{C3} = C_3 \frac{dv_{C3}}{dt} = i_{L2} - i_{L1} \end{cases} \quad (2)$$

By applying volt-second and amp-second balances to L_1 , L_2 , and C_3 , we have

$$D(v_{C3}) + (1-D)(-V_2 - V_1 + v_{C3}) = 0 \quad (3)$$

$$D(V_1) + (1-D)(V_1 - v_{C3}) = 0 \quad (4)$$

$$D(-i_{L1}) + (1-D)(i_{L2} - i_{L1}) = 0 \quad (5)$$

where D represents the duty cycle of S_1 and S_3 .

By using (4), the average voltage across C_3 can be determined as

$$v_{C3} = \frac{1}{1-D} V_1 \quad (6)$$

From (3) and (6), the voltage conversion ratio of the proposed converter during the forward direction mode can be calculated as follow

$$M_{CCM\{forward\}} = \frac{V_2}{V_1} = \frac{D(D-2)}{(1-D)^2} \quad (7)$$

TABLE 1 Comparison among main Bidirectional dc-dc Converters.

Ref.	Number of Elements [†]	Conducting Switch at F and B [‡]	Forward M_{CCM} range	Backward M_{CCM} range	Main test results, Direct Connection of Input and Output (DCIO)?
Proposed	4 S	F: 2,2,1	$\frac{D(D-2)}{(1-D)^2}$	$\frac{-D^2}{1-D^2}$	40Vdc, 180Vdc
	2 L, 3 C	B: 2,2,1	0-∞	0-∞	500 W, 20kHz η_{max} : 97.6% DCIO: ✓
[11]	4 S	F: 2,2	$\frac{D}{1-D}$	$\frac{D}{1-D}$	NA
	1 L, 2 C	B: 2,2	0-∞	0-∞	20 kW, 16kHz η_{max} : 92% DCIO: ✓
[18]	3 S	F: 2,2	$\frac{2D}{1-D}$	$\frac{0.5D}{1-D}$	85Vdc, 396Vdc
	2 L, 4 C	B: 2,2	0-∞	0-∞	1.6 kW, 100kHz η_{max} : 97.6% DCIO: ×
[23]	4 S	F: 2,2,1	$(\frac{D}{1-D})^2$	$(\frac{D}{1-D})^2$	40Vdc, 400Vdc
	3 L, 4 C	B: 2,2,1	0-∞	0-∞	500 W, 50kHz η_{max} : 97.8% DCIO: ✓
[19]	6 S, 2 D	F: 3,2	$\frac{2D}{1-D}$	$\frac{0.5D}{1-D}$	50Vdc, 95Vdc
	2 L, 1 C	B: 3,2	0-∞	0-∞	100 W, 50kHz η_{max} : 94% DCIO: ×
[16]	4 S	F: 2,2	$\frac{2}{1-D}$	$\frac{D}{2}$	40Vdc, 300Vdc
	1 L, 4 C	B: 2,2	2-∞	0-0.5	300 W, 20kHz η_{max} : 94% DCIO: ✓
[24]	5 S	F: 2,2	$\frac{2}{1-D}$	$\frac{D}{2}$	50Vdc, 400Vdc
	2 L, 4 C	B: 2,3	2-∞	0-0.5	1 kW, 20kHz η_{max} : 95.3% DCIO: ×
[21]	4 S	F: 2,2	$(\frac{D}{1-D})^2$	$(\frac{D}{1-D})^2$	36Vdc, 100Vdc
	3 L, 4 C	B: 2,2	0-∞	0-∞	100 W, 50kHz η_{max} : 91.83% DCIO: ✓
[20]*	6 S	F: 3,2	$(\frac{D}{1-D})^2$	$(\frac{D}{1-D})^2$	20Vdc, 38.7Vdc
	3 L, 4 C	B: 3,2	0-∞	0-∞	133 W, 40kHz η_{max} : NA DCIO: ✓
[15]	6 S	F: 3,3	$\frac{4}{1-D}$	$\frac{D}{4}$	20Vdc, 270Vdc
	2 L, 5 C	B: 3,3	4-∞	0-0.25	500 W, 100kHz η_{max} : 91.83% DCIO: ✓
[25]	5 S	F: 2,3,1	$\frac{1+D}{(1-D)^2}$	$\frac{D^2}{2-D}$	40Vdc, 200Vdc
	2 L, 4 C	B: 3,2,1	1-∞	0-1	500 W, 50kHz η_{max} : 97.2% DCIO: ✓

(Continues)

TABLE 1 (Continued)

Ref.	Number of Elements [†]	Conducting Switch at F and B [‡]	Forward M_{CCM} , range	Backward M_{CCM} , range	Main test results, Direct Connection of Input and Output (DCIO)?
[14]	4 S 1 L, 3 C	F: 2,2 B: 2,2	$\frac{2}{1-D}$ 2- ∞	$\frac{D}{2}$ 0-0.5	14Vdc, 42Vdc 140 W, 20–70kHz η_{max} : 97.5% DCIO: ✓

[†]S: switch, D: diode, SD: series body diode, L: inductor, C: capacitor.

[‡]F: forward direction, B: backward direction.

*Bidirectional version.

TABLE 2 RMS value of Total Voltage and Current Stress.

Ref.	TVS _{RMS} /V _{1,rms}	TCS _{RMS} /i _{L,rms}
	Forward direction, Backward direction	Forward direction, Backward direction
Proposed	$\frac{2-D}{(1-D)^2} (\sqrt{D} + \sqrt{1-D})$ $\frac{1+D}{D^2} (\sqrt{D} + \sqrt{1-D})$	$\frac{\sqrt{D+\sqrt{1-D}}}{D}$ $\frac{\sqrt{D+\sqrt{1-D}}}{D^2}$
[23]	$\frac{(1+D)\sqrt{D+\sqrt{1-D}}}{(1-D)^2}$ $\frac{\sqrt{D+(2-D)\sqrt{1-D}}}{D^2}$	$\frac{\sqrt{D+\sqrt{1-D}}}{D^2}$ $\frac{[(1-D)+ 2D-1]\sqrt{D+\sqrt{1-D}}}{(1-D)^2}$
[25]	$\frac{(4-2D)\sqrt{D+2\sqrt{1-D}}}{(1-D)^2}$ $\frac{3\sqrt{D+(2+D)\sqrt{1-D}}}{1+D}$	$\frac{(3-D)\sqrt{D+2\sqrt{1-D}}}{1+D}$ $\frac{3\sqrt{D+(2+D)\sqrt{1-D}}}{1+D}$
[16]	$\frac{2\sqrt{D+2\sqrt{1-D}}}{1-D}$ $\frac{2\sqrt{D+2\sqrt{1-D}}}{D}$	$\frac{1}{D}\sqrt{D+4\sqrt{1-D}}$ $\sqrt{D} + \frac{1}{D}\sqrt{1-D}$
[18]	$\frac{2\sqrt{D+\sqrt{1-D}}}{1-D}$ $\frac{2\sqrt{D+\sqrt{1-D}}}{D}$	$\frac{\sqrt{D+\sqrt{1-D}}}{D}$ $\frac{\sqrt{D+\sqrt{1-D}}}{D}$
[21]	$\frac{\sqrt{D+\sqrt{1-D}}}{(1-D)^2}$ $\frac{\sqrt{D+\sqrt{1-D}}}{(1-D)^2}$	$\frac{\sqrt{D+\sqrt{1-D}}}{D^2}$ $\frac{\sqrt{D+\sqrt{1-D}}}{D^2}$
[11]	$\frac{\sqrt{D+\sqrt{1-D}}}{1-D}$ $\frac{\sqrt{D+\sqrt{1-D}}}{1-D}$	$\frac{2\sqrt{D+2\sqrt{1-D}}}{D}$ $\frac{2\sqrt{D+2\sqrt{1-D}}}{D}$

Furthermore, the primary side average current is

$$\bar{i}_1 = \frac{D(D-2)}{1-D} \quad \bar{i}_{L1} = D(D-2) \bar{i}_{L2} \quad (8)$$

State 3 of DCM [t_2 - t_3]: According to Figure 3(c), in this mode, the current through inductor L_1 meets zero at time t_2 , and the current through L_2 meets zero at time t_3 , both before the end of the switching period.

State 4 of DCM [t_3 - T_s]: In this mode, all of the power switches are turned off. The current through both inductors remains. An entire period T_s has been completed after this interval.

Considering these intervals, one can define D_1 and D_2 as duty cycles where the current of L_1 and L_2 becomes zero, respectively. In this regard, according to a typical DCM waveform in Figure 5(a), the voltage across the inductors can be defined as;

$$v_{L1} = \begin{cases} v_{C3} & 0 \leq t < DT_s \\ v_{C3} - V_1 - V_2 & DT_s \leq t < (D+D_1)T_s \\ 0 & (D+D_1)T_s \leq t < T_s \end{cases} \quad (9)$$

$$v_{L2} = \begin{cases} V_1 & 0 \leq t < DT_s \\ -v_{C3} + V_1 & DT_s \leq t < (D+D_2)T_s \\ 0 & (D+D_2)T_s \leq t < T_s \end{cases} \quad (10)$$

Now, the volt-second balance is applied to both inductors. So, the voltage of capacitor C_3 is

$$v_{C3} = \frac{D+D_2}{D_2} V_1 \quad (11)$$

As a result, the DCM voltage gain transfer ratio during the forward direction mode can be obtained as

$$M_{DCM\{forward\}} = \frac{V_2}{V_1} = \frac{D^2 + DD_2 + DD_1}{D_1 D_2} \quad (12)$$

2.2 | Backward direction operation mode

In the backward direction operation or the charging mode, the power flows from V_2 to V_1 . Two states associated with CCM and four states associated with DCM operation modes are defined as follows.

State 1 of CCM and DCM [0 - t_1]: During $0 \leq t < DT_s$ or state-1 of the backward operation mode and according to Figure 3(d), S_2 and S_4 are turned on, while S_1 and S_3 are turned off. In this state, L_1 and L_2 are charged by the input dc source V_2 . Thus, the current through L_1 and L_2 increases, whereas the energy of C_3 is released through L_2 and V_1 . According to the typical time-domain waveforms in Figure 4(b), the derived current and voltage equations are as follows:

$$\begin{cases} v_{L1} = L \frac{dI_{L1}}{dt} = V_2 + V_2 - v_{C3} \\ v_{L2} = L \frac{dI_{L2}}{dt} = -V_1 + v_{C3} \\ i_{C3} = C_3 \frac{dv_{C3}}{dt} = i_{L2} - i_{L1} \end{cases} \quad (13)$$

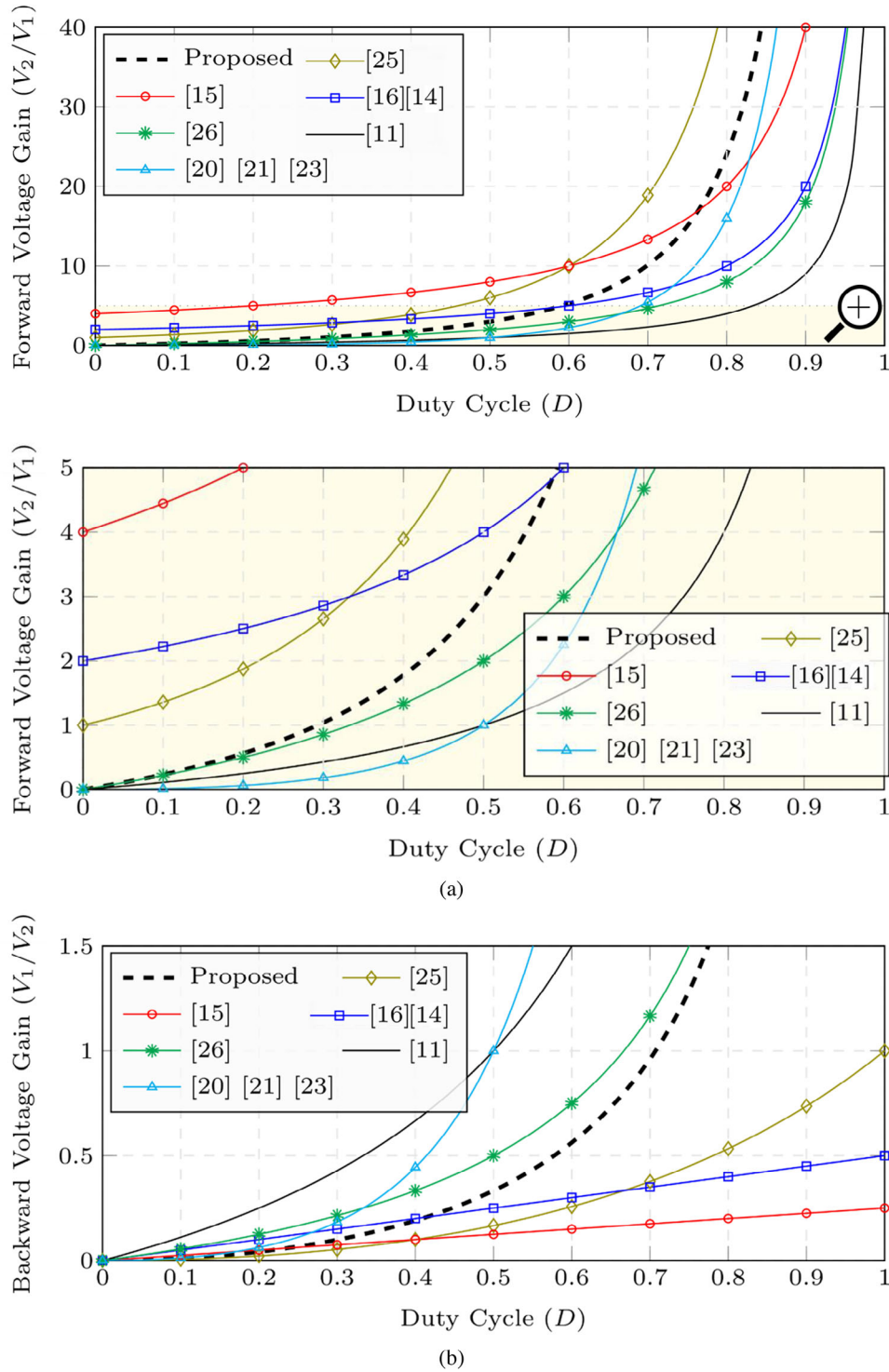


FIGURE 6 Voltage gain ratio in: (a) forward and (b) backward directions.

State 2 of CCM [t_1 - T_s] and DCM [t_1 - t_2]: Contrary to state 1, during this interval, as shown in Figure 3(e), S_2 and S_4 are turned off whereas the body diodes of S_1 and S_3 are conducting. The inductor L_2 releases its energy into the primary side voltage through the body diode of S_3 . Similarly, L_1 releases energy into C_3 through the body diode of S_1 . Therefore, we have:

$$\begin{cases} v_{L1} = L \frac{dL_1}{dt} = -v_{C3} \\ v_{L2} = L \frac{dL_2}{dt} = -V_1 \\ i_{C3} = C_3 \frac{dv_{C3}}{dt} = i_{L1} \end{cases} \quad (14)$$

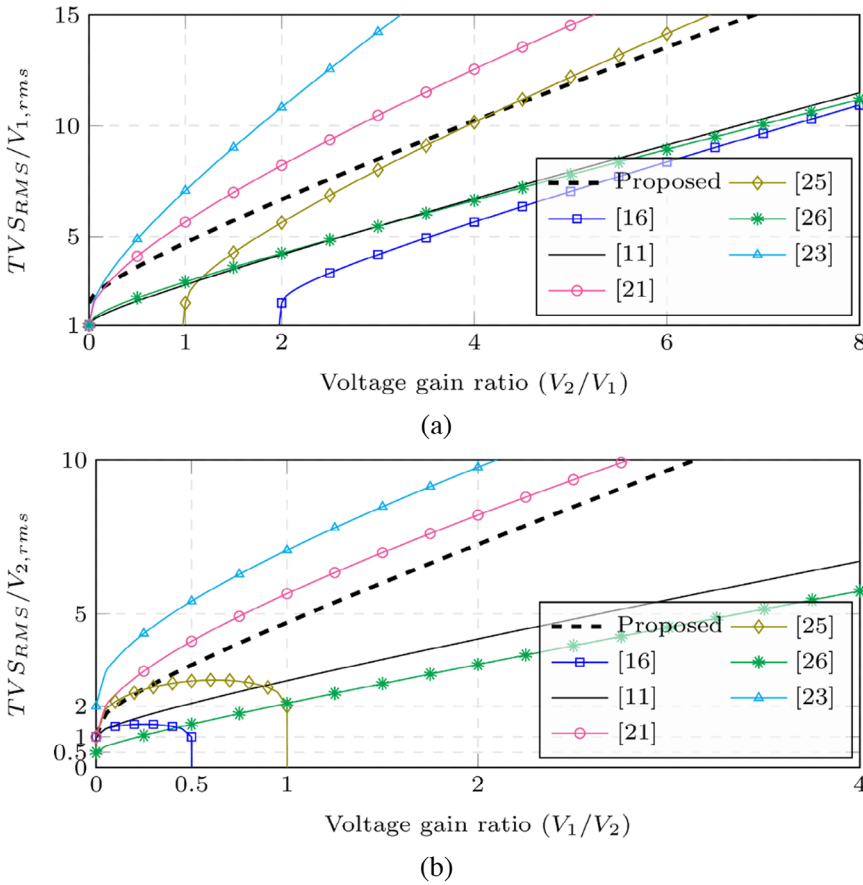


FIGURE 7 RMS value of TVS during: (a) Forward and (b) Backward directions.

By applying volt-second and amp-second balances to L_1 , L_2 , and C_3 , we have

$$D(V_1 + V_2 - v_{C3}) + (1 - D)(-v_{C3}) = 0 \quad (15)$$

$$D(-V_1 + v_{C3}) + (1 - D)(-V_1 - v_{C3}) = 0 \quad (16)$$

$$D(-i_{L1}) + (1 - D)(i_{L2} - i_{L1}) = 0 \quad (17)$$

By using (16), the average voltage across C_3 can be determined as

$$\overline{v_{C3}} = \frac{1}{D} V_1 \quad (18)$$

From (15) and (18), in the backward direction mode the voltage conversion ratio of the proposed converter can be calculated as follow

$$M_{CCM\{backward\}} = \frac{V_1}{V_2} = \frac{-D^2}{1 - D^2} \quad (19)$$

Furthermore, the primary side average current is

$$i_1 = \frac{1 - D^2}{D} i_{L1} = (1 - D^2) i_{L2} \quad (20)$$

State 3 of DCM [t_2 - t_3]: According to Figure 3(f), in this mode, the current through inductor L_1 meets zero at time t_2 , and the

current through L_2 meets zero at time t_3 , both before the end of the switching period.

State 4 of DCM [t_3 - T_s]: In this mode, all of the power switches are turned off. The current through inductors meets zero. At the end of this interval, a complete period T_s has been passed.

Considering these intervals, one can define D_1 and D_2 as duty cycles where the current of L_1 and L_2 becomes zero, respectively. In this regard, according to a typical DCM waveform in Figure 5(b), the voltage across the inductors can be defined as

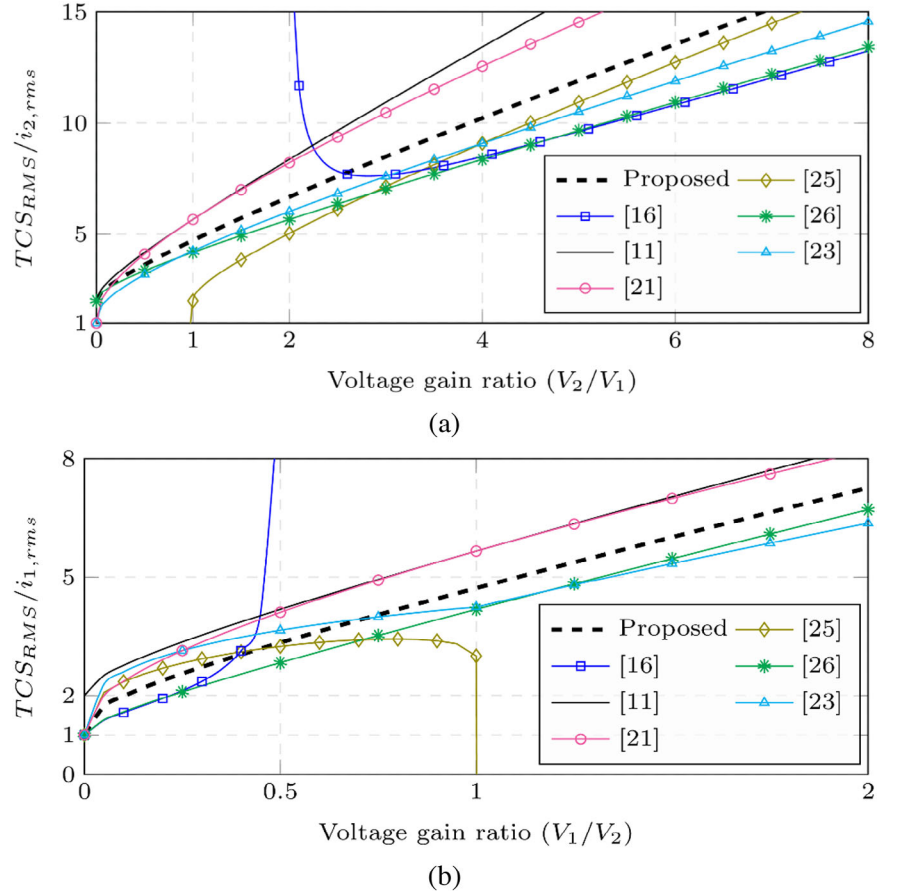
$$v_{L1} = \begin{cases} V_1 + V_2 - v_{C3} & 0 \leq t < DT_s \\ -v_{C3} & DT_s \leq t < (D + D_1)T_s \\ 0 & (D + D_1)T_s \leq t < T_s \end{cases} \quad (21)$$

$$v_{L2} = \begin{cases} -V_1 + v_{C3} & 0 \leq t < DT_s \\ -V_1 & DT_s \leq t < (D + D_2)T_s \\ 0 & (D + D_2)T_s \leq t < T_s \end{cases} \quad (22)$$

Now, the volt-second balance is applied to both inductors. So, the voltage of capacitor C_3 is

$$v_{C3} = \frac{D + D_2}{D} V_1 \quad (23)$$

FIGURE 8 RMS value of TCS during: (a) Forward and (b) Backward directions.



As a result, the DCM voltage gain transfer ratio during the backward direction mode can be obtained as

$$M_{DCM\{backward\}} = \frac{V_1}{V_2} = \frac{D^2}{DD_1 + DD_2 + D_1D_2} \quad (24)$$

3 | DESIGN CONSIDERATIONS

3.1 | Passive components design

By considering a switching frequency, f_s , the current ripple of inductors Δi_{L1} and Δi_{L2} and the voltage ripple of capacitor Δv_{C3} the value of the passive components can be obtained as follows

$$Forward : \begin{cases} L_1 = \frac{DV_1}{(1-D)\Delta i_{L1}f_s} \\ L_2 = \frac{DV_1}{\Delta i_{L2}f_s} \\ C_3 = \frac{(1-D)i_1}{(2-D)\Delta v_{C3}f_s} \end{cases} \quad (25)$$

$$Backward : \begin{cases} L_1 = \frac{D(1-D)V_2}{(1-D^2)\Delta i_{L1}f_s} \\ L_2 = \frac{(1-D)^2V_2}{(1-D^2)\Delta i_{L2}f_s} \\ C_3 = \frac{D(1-D)i_1}{(1-D^2)\Delta v_{C3}f_s} \end{cases} \quad (26)$$

Moreover, the minimum value of inductor currents must be positive for CCM, and the critical value of L_1 and L_2 can be expressed as

$$Forward : \begin{cases} L_1 \geq \frac{(2-D)D^2V_1}{(1-D)^2i_1f_s} \\ L_2 \geq \frac{(2-D)D^2V_1}{i_1f_s} \end{cases} \quad (27)$$

$$Backward : \begin{cases} L_1 \geq \frac{(1-D)(1-D^2)V_1}{D^2i_1f_s} \\ L_2 \geq \frac{(1-D)V_1}{(1-D^2)i_1f_s} \end{cases} \quad (28)$$

The capacitor C_2 performs as a buffer for the instantaneous power difference between the ac grid and the proposed dc-dc converter. Thus, to maintain the ripple of the dc-link voltage (ΔV_2) below a specific value, the required C_2 is:

$$C_2 = \frac{P_b}{\omega_0 V_2 \Delta V_2} \quad (29)$$

where P_b is the average output power of battery side and ω_0 is the grid angular frequency.

The grid side filter inductor i.e., L_g is designed according to the ac source voltage, the dc/ac converter modulation index,

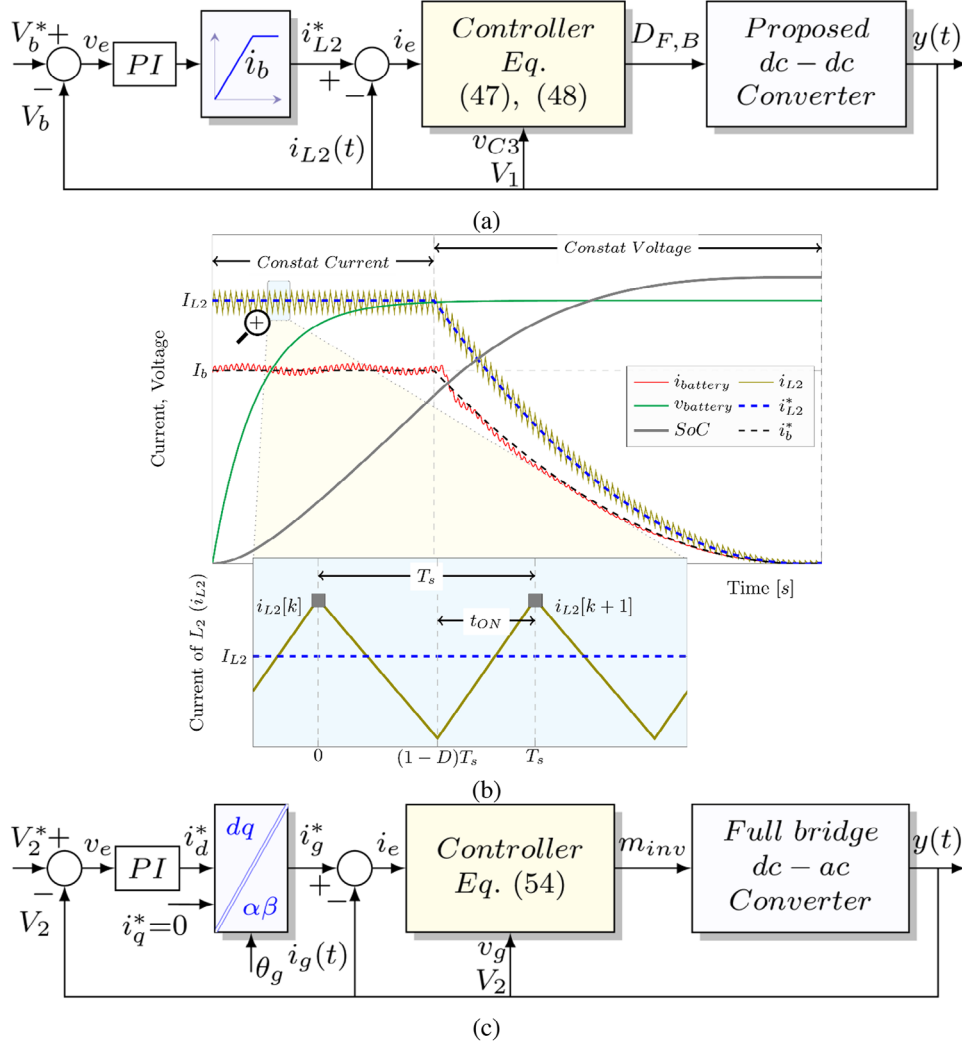


FIGURE 9 (A) dc-dc stage control loop, (B) battery current variations during CC and CV modes, and (C) dc-ac stage control loop.

m_{inv} and the desired current ripple, Δi_g as

$$L_g = \frac{v_g (1 - m_{inv}) T_s}{\Delta i_g} \quad (30)$$

As an example considering $P_b = 500$ W, $v_g = 110\sqrt{2} \sin \omega_0 t$, $V_1 = 40$ V, $V_2 = 180$ V, and $f_s = 20$ kHz the values of $L_1 = 1.5$ mH and $L_2 = 1$ mH satisfy (25)–(28) for a current ripple less than 30% and 10% for L_1 and L_2 , respectively. Considering 20% voltage ripple across C_3 , the value of $10 \mu\text{F}$ satisfies the above equations, and the choice of components for the dc-ac stage is $C_2 = 0.98$ mF and $L_g = 4$ mH.

3.2 | Semiconductors rating

The average (over a switching cycle) on-state current and average off-state voltage across the switches and the diode can be expressed as:

$$\text{Forward : } \begin{cases} V_{S1} = \frac{1}{(1-D)^2} V_1 \\ V_{S2} = \frac{1}{(1-D)^2} V_1 \\ V_{S3} = \frac{1}{(1-D)} V_1 \\ V_{S4} = \frac{1}{(1-D)} V_1 \end{cases}, \begin{cases} I_{S1} = \frac{1-D}{D(2-D)} I_1 \\ I_{S2} = \frac{1-D}{D(2-D)} I_1 \\ I_{S3} = \frac{1}{D(2-D)} I_1 \\ I_{S4} = \frac{1}{D(2-D)} I_1 \end{cases} \quad (31)$$

$$\text{Backward : } \begin{cases} V_{S1} = \frac{1}{D^2} V_1 \\ V_{S2} = \frac{1}{D^2} V_1 \\ V_{S3} = \frac{1}{D} V_1 \\ V_{S4} = \frac{1}{D} V_1 \end{cases}, \begin{cases} I_{S1} = \frac{D}{1-D^2} I_1 \\ I_{S2} = \frac{D}{1-D^2} I_1 \\ I_{S3} = \frac{1}{1-D^2} I_1 \\ I_{S4} = \frac{1}{1-D^2} I_1 \end{cases} \quad (32)$$

Therefore, the rms value of total current stress (TCS) and total voltage stress (TVS) of semiconductor devices are

TABLE 3 Pros and Cons of main Bidirectional Converters.

Ref.:	Pros (✓) and Cons (×)
Proposed	<ul style="list-style-type: none"> ✓ High voltage gain ratio ✓ Boundless buck-boost voltage gain ratio ✓ Direct connection of input and output terminals ✓ Low EMI issues ✓ Low TVS ✓ Low TCS × High number of semiconductor devices
[11]	<ul style="list-style-type: none"> × Lower voltage gain ratio ✓ Boundless buck-boost voltage gain ratio ✓ Direct connection of input and output terminals ✓ Low EMI issues ✓ Lower TVS × Higher TCS × High number of semiconductor devices
[18]	<ul style="list-style-type: none"> × Lower voltage gain ratio ✓ Boundless buck-boost voltage gain ratio × No direct connection of input and output terminals × High EMI issues ✓ Lower TVS ✓ Lower TCS ✓ Lower number of semiconductor devices
[23]	<ul style="list-style-type: none"> × Lower voltage gain ratio ✓ Boundless buck-boost voltage gain ratio ✓ Direct connection of input and output terminals ✓ Low EMI issues × Higher TVS ✓ Lower TCS × High number of semiconductor devices
[16]	<ul style="list-style-type: none"> × Lower voltage gain ratio
[15]	<ul style="list-style-type: none"> × limited voltage gain ratio ✓ Direct connection of input and output terminals ✓ Low EMI issues ✓ Lower TVS ✓ Lower TCS × Higher number of semiconductor devices
[24]	<ul style="list-style-type: none"> × Lower voltage gain ratio × limited voltage gain ratio × No direct connection of input and output terminals × High EMI issues ✓ Lower TVS ✓ Lower TCS × Higher number of semiconductor devices
[21]	<ul style="list-style-type: none"> × Lower voltage gain ratio

(Continues)

TABLE 3 (Continued)

Ref.:	Pros (✓) and Cons (×)
[20]*	<ul style="list-style-type: none"> ✓ Boundless buck-boost voltage gain ratio ✓ Direct connection of input and output terminals ✓ Low EMI issues × Higher TVS × Higher TCS × High number of semiconductor devices
[25]	<ul style="list-style-type: none"> ✓ Higher voltage gain ratio × limited voltage gain ratio ✓ Direct connection of input and output terminals ✓ Low EMI issues × Higher TVS ✓ Lower TCS × Higher number of semiconductor devices

*Bidirectional version

$$Forward : \begin{cases} IV S_{rms} = (\sqrt{D} + \sqrt{1-D}) \frac{2-D}{(1-D)^2} V_1 \\ TC S_{rms} = (\sqrt{D} + \sqrt{1-D}) \frac{1}{D} i_{1,rms} \end{cases} \quad (33)$$

$$Backward : \begin{cases} IV S_{rms} = (\sqrt{D} + \sqrt{1-D}) \frac{1+D}{D^2} V_1 \\ TC S_{rms} = (\sqrt{D} + \sqrt{1-D}) \frac{1}{1-D} i_{1,rms} \end{cases} \quad (34)$$

4 | COMPARISON OF THE PROPOSED DC-DC CONVERTER TO THE STATE OF THE ART

The main achievements and the characteristics of the EV bidirectional dc-dc converters and the proposed converter are summarized in Table 1.

The main point of Table 1 is that among all the buck-boost bidirectional converters which do not have a gain limitation the proposed converter has the highest boundless voltage gain ratio. The converters with higher gain ratios all have a limitation on their gain in both directions. The proposed bidirectional dc-dc converter has four semiconductor devices and adopts two of them during each state of operation.

The total semiconductor device count of buck-boost bidirectional dc-dc converters i.e. the converters in [11, 18, 23, 19, 21, and 20] is 4, 3, 4, 8, 4, and 6, respectively and for the proposed converter it is 4. Although the total semiconductor device count of converter in [18] is lower than the proposed converter, the voltage gain ratio of [18] is lower than the proposed converter in both directions. Furthermore, unlike the proposed converter, there is no direct connection between input and output terminals in the converter of [18] which leads to increased EMI issues.

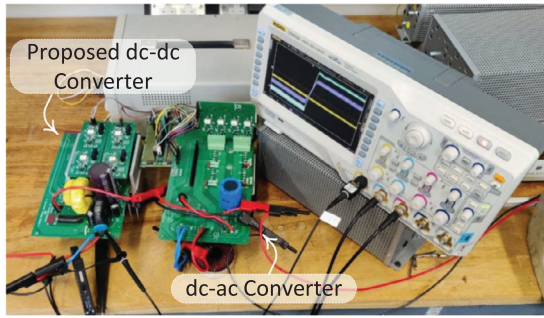


FIGURE 10 Experimental prototype of the proposed EV onboard charger.

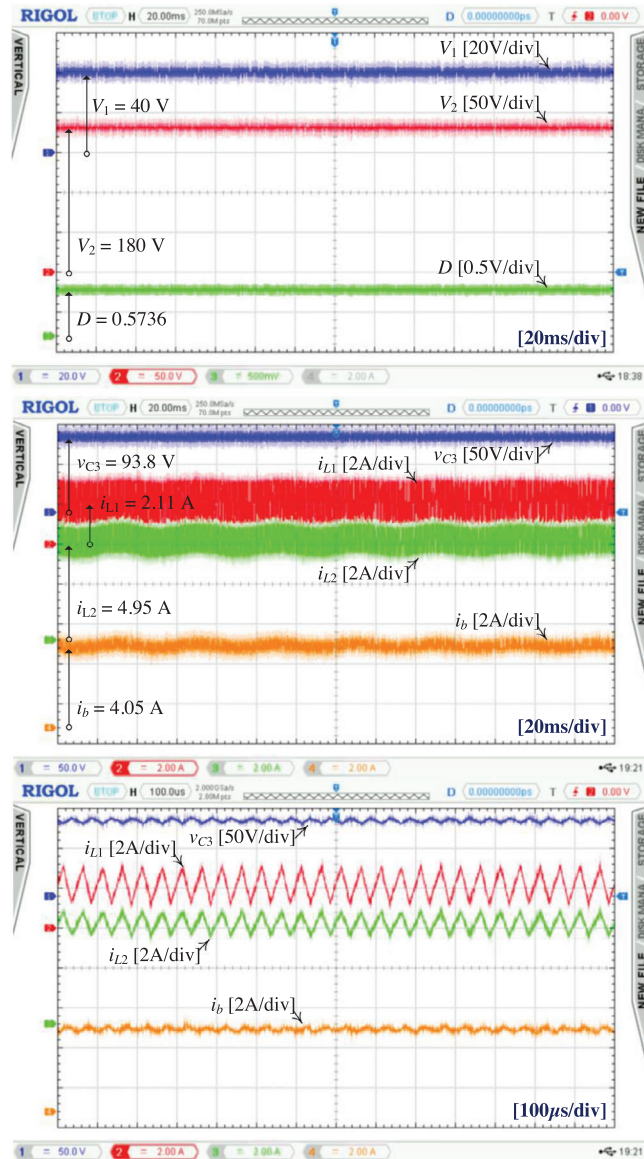


FIGURE 11 Waveforms of V_1 , V_2 , D , v_{C3} , i_{L1} , i_{L2} , and i_b for the CCM operation of forward direction mode.

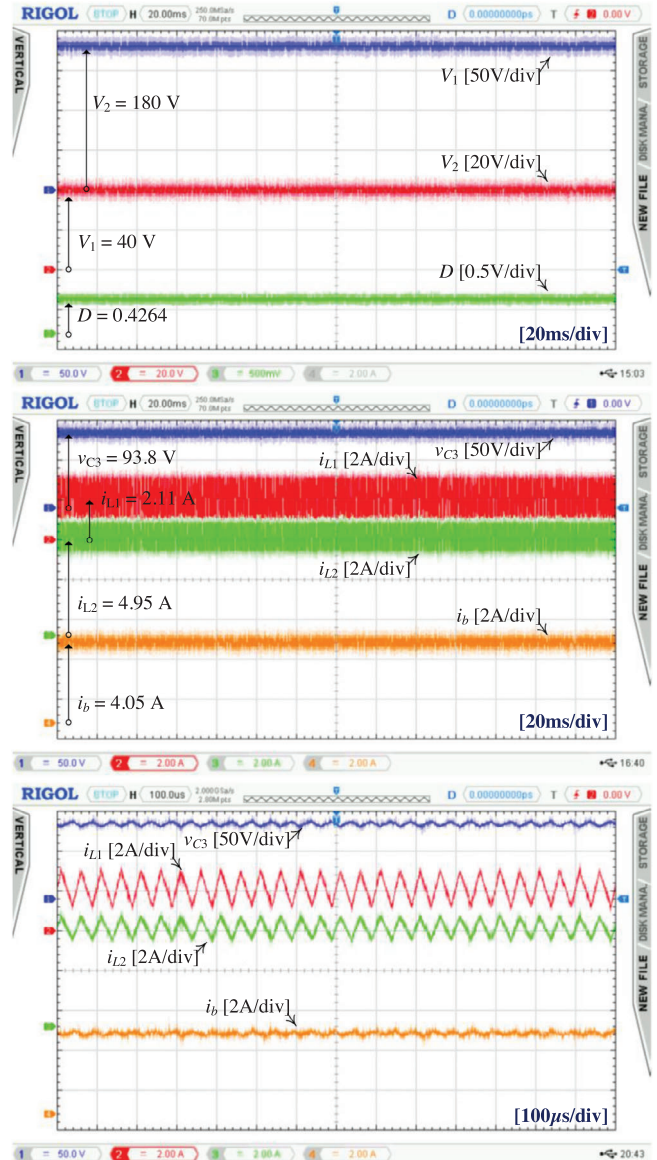
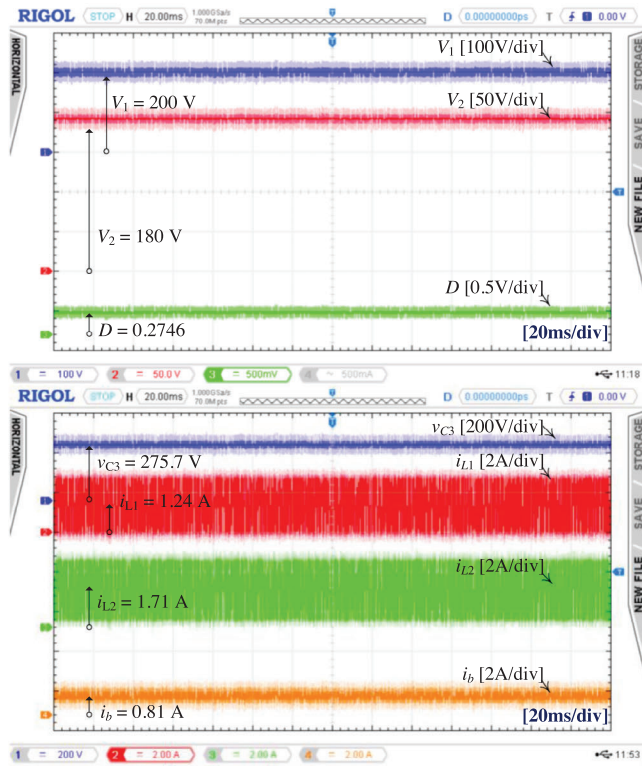
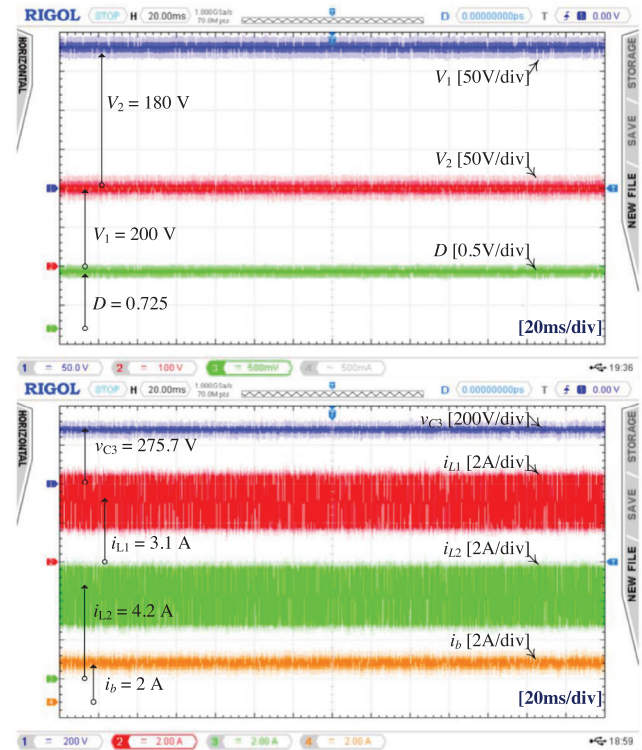


FIGURE 12 Waveforms of V_1 , V_2 , D , v_{C3} , i_{L1} , i_{L2} , and i_b for the CCM operation of backward direction mode.

The voltage gain ratios of forward and backward directions versus duty cycle have been depicted in Figure 6. As shown in Figure 6(a), in the forward direction, only the voltage gain ratio of converters in [25, 15, and 16] is higher than the proposed converter. However, the dc output voltage of [25, 15, and 16] is limited to the range 1 to ∞ , from 2 to ∞ , and from 4 to ∞ , respectively and the proposed converter has a wide voltage gain ratio. Similarly, although in the backward direction, the converters in [25, 15, and 16] have higher step-down voltage gain ratios, their output dc voltage gain range is limited to 0 to 0.25, 0 to 0.5, and 0 to 1, and the voltage gain ratio of the proposed converter is boundless. Therefore, these converters are not particularly suitable for the application because of their limited voltage range.



(a)



(b)

FIGURE 13 Waveforms of V_1 , V_2 , D , v_{C3} , i_{L1} , i_{L2} , and i_b for stepdown mode of (a) forward and (b) backward directions.

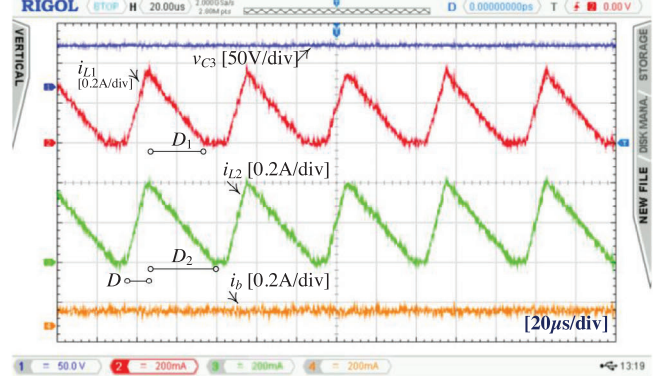
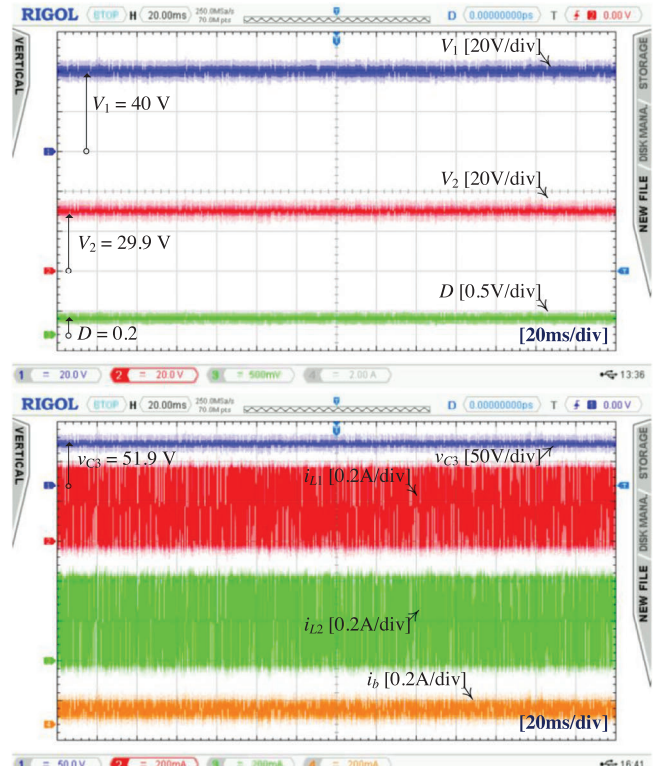


FIGURE 14 Voltage and current of input, output, and inductors during DCM mode of forward direction.

The term “wide voltage gain” signifies that by adjusting the duty cycle within the range of 0 to 1.0, the proposed converter inherently covers the entire spectrum of possible voltage gain ratios. This inherent feature gives the proposed converter a significant advantage by allowing it to meet a wide range of voltage gain requirements. As a result, the proposed converter outperforms the limitations observed in the converters discussed in references [15, 16, 24, 25].

Another comparison can be made between the proposed bidirectional dc-dc converter and its main competitors based on the normalized rms value of total voltage stress (TVS_{rms}) and the normalized rms value of total current stress of semiconductor devices (TCS_{rms}). The comparisons are presented in Table 2 and shown in Figures 7 and 8, respectively where

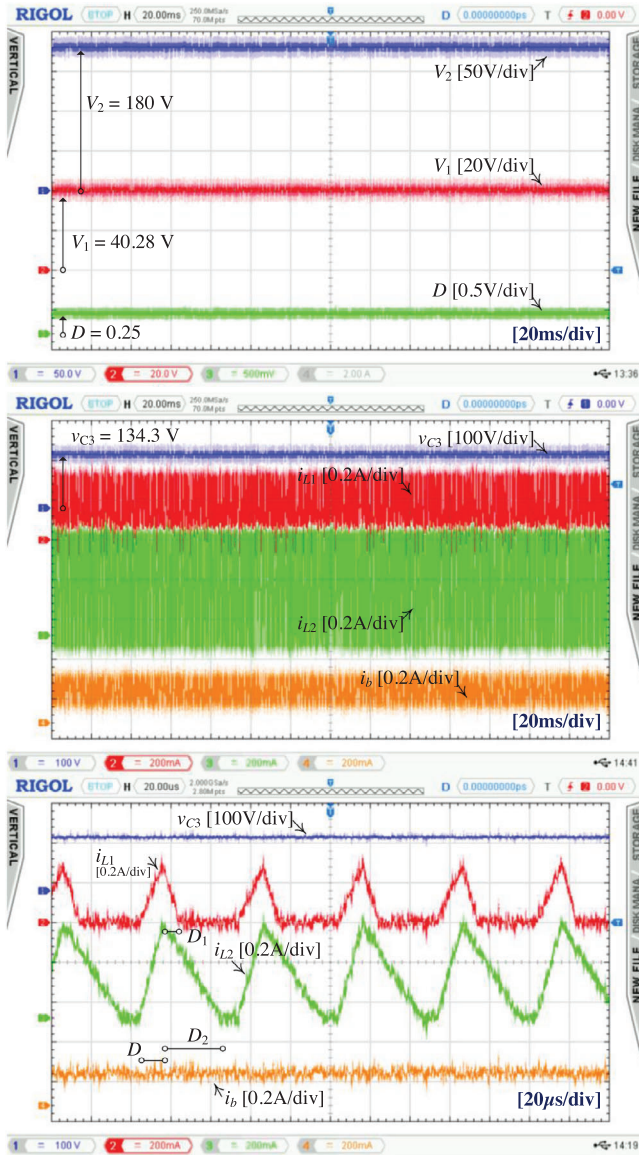


FIGURE 15 Voltage and current of input, output, and inductors during DCM mode of backward direction.

the TVS and TCS are plotted vs voltage gain ratio. In a wide range of voltage gain ratios, the proposed converter can perform better than some of the previous bidirectional converters. For example the proposed converter offers a lower TVS_{rms} than converters in [21, 23, and 25] when the voltage gain is higher than 4 and lower than 0.25 for forward and backward directions, respectively. Furthermore, the normalized TCS of the proposed converter is lower than the converters in [11 and 21].

It is also useful to compare the conducting semiconductor device count of the proposed converter and the main competitor approaches. As shown in Table 1, it is clear that the proposed converter has only two conducting switches during each direction which is similar to the lowest number used by any other converter in the table.

It is also worth noting that, unlike the previously published buck-boost bidirectional dc-dc converter except [11], the pro-

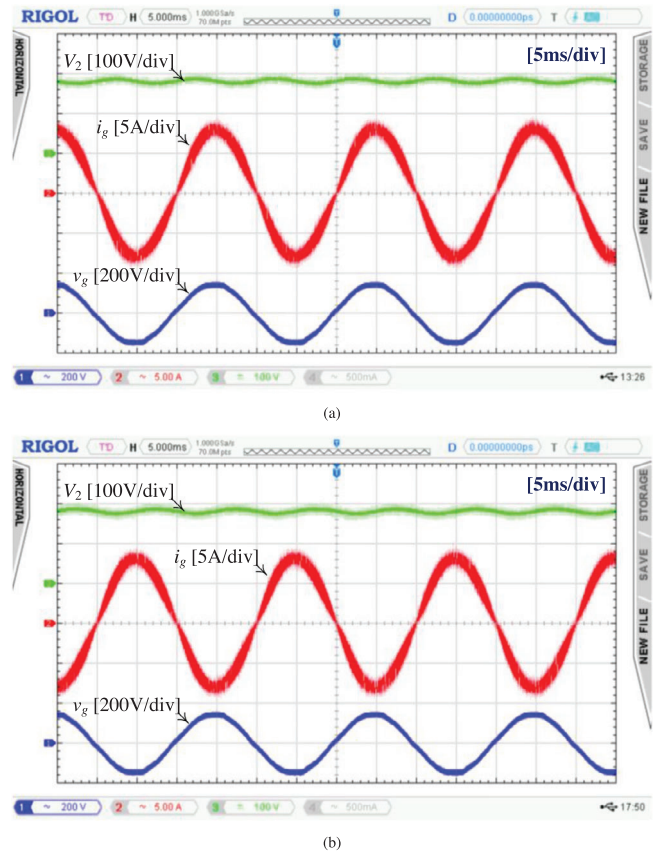


FIGURE 16 Grid connected operation: (a) forward (V2G) and (b) backward (G2V) direction mode.

posed converter uses only three capacitors and two inductors in the structure which can reduce the volume and cost of the EV charger.

Further, the proposed converter has a maximum efficiency of 97.6%, as will be shown in section 6. As a result, the proposed converter has a good balance between component count, semiconductor device ratings, and efficiency, making it a very practical power converter solution for EV chargers.

In Table 3, the analysis of various bidirectional dc-dc converters reveals that the proposed converter possesses a distinct set of advantages. Notably, it excels in its capacity to perform buck-boost operation, enabling effective voltage regulation across a wide range of input voltages.

Although the converter in [25] offers a higher voltage gain ratio than the proposed converter, it's essential to note that the former lacks a restricted voltage gain ratio. In simpler terms, the converter in [25] does not function within the gain voltage range of 0 to 1 (or 1 to ∞) during its forward (or backward) mode of operation. This limitation sets the proposed converter apart, as it maintains a well-defined voltage gain ratio under these conditions.

Furthermore, an additional advantage of the proposed converter is its capability to effectively address EMI noise issues. This is achieved through the establishment of a direct connection between the input and output terminals. By doing so, the converter offers an inherent mechanism for managing

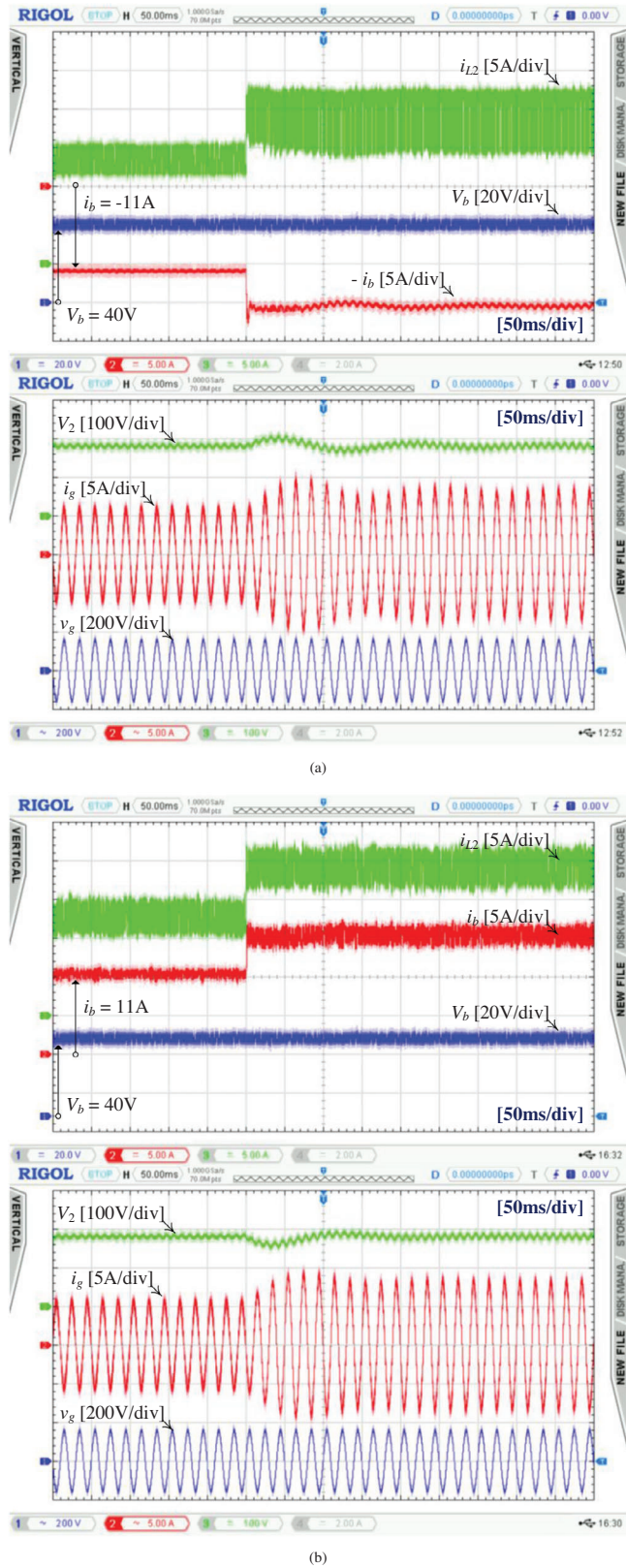


FIGURE 17 Transient response to a step change of i_b (a) forward (V2G) and (b) backward (G2V) direction mode.

EMI noise, contributing to its overall robustness and reliable performance.

In summary, the proposed bidirectional dc-dc converter distinguishes itself through its buck-boost functionality, accommodating a broad input voltage range. While other converters might offer higher voltage gain ratios, the proposed converter's well-defined gain ratio across all operational ranges, coupled with its ability to mitigate EMI noise, positions it as a noteworthy solution in the field. The proposed converter stands out with its unique ability to both step-up and step-down voltage. In contrast to many existing converters that are typically either buck or boost converters, this versatility provides flexibility to address a wide spectrum of input and output voltage requirements. Moreover, the converter's design includes the capability to handle a broad input voltage range, making it well-suited for applications where input voltage fluctuations are substantial, a feature not commonly found in bidirectional converters with limited input voltage ranges.

However, Table 3 contains a list of converters that are all categorized as non-isolated EV chargers. This implies that none of the converters in this study, including the proposed one, have inherent isolation between the battery and the DC-link. The practicality of addressing the isolation requirement lies in the flexibility of EV charger design. In real-world applications, a high-frequency transformer can be employed at the output stage of any of the converters listed in Table 3. This transformer can effectively provide the necessary isolation, ensuring the safety of the system and users during charging.

5 | PROPOSED CONTROL SYSTEM DESIGN

The control system of the proposed EV charger includes the control loop of the battery side current and the grid side current during both forward and backward directions. In this paper for both stages we have adopted two dead-beat control loops [26, 27] to regulate both battery side voltage and current in dc-dc stage and dc-link voltage and ac grid current in dc-ac stage.

5.1 | dc-dc stage control system

The control of the proposed dc-dc converter includes the current control of the battery during the constant current (CC) loop and the voltage control of the battery during constant voltage (CV) loop. The overall diagram of the proposed control system is shown in Figure 9. In this converter, a digital dead-beat indirect current control concept is adopted for both directions. The battery-side voltage reference V_b^* is usually set as the full-charge voltage of the battery. When the battery is not fully charged, the battery current reference i_b^* is determined. In this situation, the output of the PI compensator in the CC/CV control loop is saturated by the limiter and the battery current

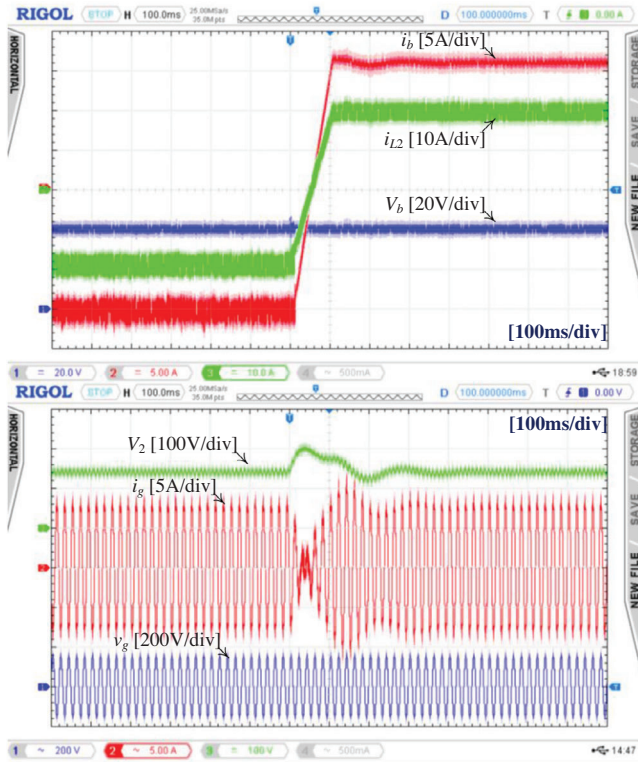


FIGURE 18 Transient waveforms from V2G to G2V.

reference is determined by the upper limit value of the limiter. When V_b reaches the full-charge voltage, the voltage control loop is activated by the PI compensator to regulate the battery voltage.

The outputs of the PI compensator and limiter become the reference for the battery side current i_b^* . Given this reference value, the reference value for the L_2 current can be calculated using $(i_{L,ref})$. From this the indirect dead-beat control system is able to calculate the optimal duty cycle for the dc-dc stage to regulate battery side voltage or current.

$$i_{L2}^* = \frac{V_1 + V_2}{V_2} \times i_b^* \quad (35)$$

As will be shown, the proposed indirect dead-beat current controller can also simply determine the optimal duty cycle for both directions from the measured V_1 and v_{C3} voltages, and measured and reference current through the L_2 inductance.

In the forward direction mode, when S_1 and S_3 are on, the voltage across L_2 can be determined as

$$v_{L2} = L_2 \frac{di_{L2}}{dt} = V_1 \quad (36)$$

Therefore, the slope of the L_2 current during the $S_{1,3}$ on-state in the forward direction ($\delta_{F,ON}$) is

$$\delta_{F,ON} = \frac{di_{L2}(t)}{dt} = \frac{V_1}{L_2} \quad (37)$$

When S_1 and S_3 are off and the body diodes of S_2 and S_4 are conducting, the inductor voltage is

$$v_{L2} = L_2 \frac{di_{L2}}{dt} = V_1 - v_{C3} \quad (38)$$

and the OFF-state slope of i_{L2} (i.e. when $S_{1,3}$ is OFF) ($\delta_{F,OFF}$) can be expressed as

$$\delta_{F,OFF} = \frac{di_{L2}(t)}{dt} = \frac{V_1 - v_{C3}}{L_2} \quad (39)$$

Similarly, during the backward direction mode, when the switches S_2 and S_4 are on, the voltage across L_2 can be expressed as

$$v_{L2} = L_2 \frac{di_{L2}}{dt} = V_1 - v_{C3} \quad (40)$$

and when S_2 and S_4 are off, the inductor voltage is

$$v_{L2} = L_2 \frac{di_{L2}}{dt} = V_1 \quad (41)$$

The current slope of L_2 during $S_{2,4}$ con-state ($\delta_{B,ON}$) and off-state ($\delta_{B,OFF}$) can be expressed as

$$\delta_{B,ON} = \frac{di_{L2}(t)}{dt} = \frac{V_1 - v_{C3}}{L_2} \quad (42)$$

$$\delta_{F,OFF} = \frac{di_{L2}(t)}{dt} = \frac{V_1}{L_2} \quad (43)$$

As shown in Figure 9(b), and based on predictive control theory, the inductor current i_{L2} at the next sampling time ($i_{L2}[k+1]$) can be calculated from its current value ($i_{L2}[k]$), using the on-state and off-state slopes of forward and backward direction modes, i.e.,

$$i_{L2}[k+1] = i_{L2}[k] + \delta_{F,B,ON} t_{ON} + \delta_{F,B,OFF} (1 - t_{ON}) \quad (44)$$

where t_{ON} is the $S_{1,3}$ or $S_{2,4}$ on-state dwell time.

The controller is intended to eliminate the error i_e between the reference current (i_{L2}^*) and $i_{L2}[k+1]$, which translates to

$$\begin{aligned} i_e = i_{L2}^* - i_{L2}[k+1] = 0 \rightarrow i_{L2}^* - i_{L2}[k] \\ - \delta_{F,B,ON} [D_{F,B}(t)] T_s - \delta_{F,B,OFF} [1 - D_{F,B}(t)] T_s = 0 \end{aligned} \quad (45)$$

Then, t_{ON} and consequently, the optimal duty cycle can be obtained as

$$D_{F,B}(t) = \frac{(i_{L2}^* - i_{L2}[k]) - \delta_{F,B,OFF} T_s}{(\delta_{F,B,ON} - \delta_{F,B,OFF}) T_s} \quad (46)$$

$$D_F(t) = \frac{L_2 (i_{L2}^* - i_{L2}[k]) + (-V_1 + v_{C3}) T_s}{v_{C3} T_s} \quad (47)$$

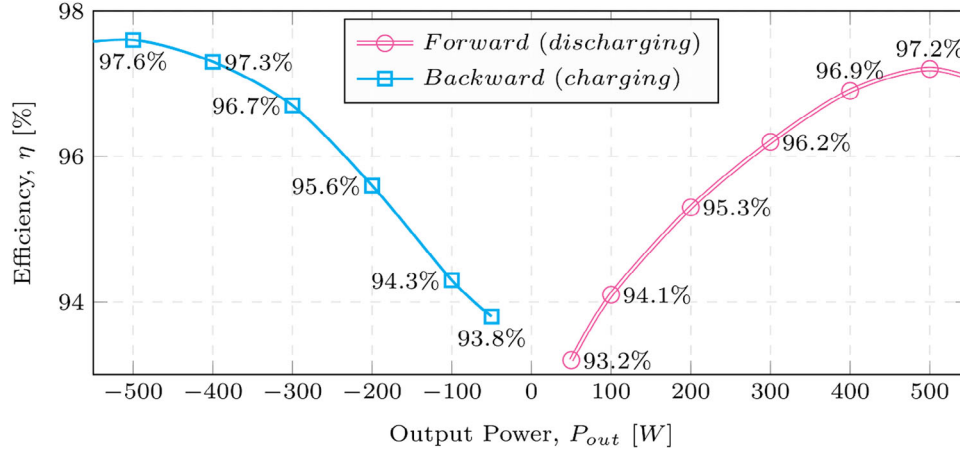


FIGURE 19 Proposed bidirectional dc-dc converter efficiency curve versus output power levels.

$$D_B(t) = \frac{L_2 (i_{L2}^* - i_{L2}[k]) - V_1 T_s}{-v_{C3} T_s} \quad (48)$$

5.2 | dc-ac stage control system

The control of the inverter used to interface with the ac grid is set up to regulate its dc-side voltage V_2 with an outer PI-based dc-voltage control loop and an inner current control loop based on dead-beat control [28, 29].

The grid side current controller aims to shape the current through L_g , denoted as i_g , as a pure sinusoid in phase with the voltage [30]. As shown in Figure 9(c) a digital dead-beat current controller [31–33] is again developed for this goal. In the dc-ac stage circuit, when S_A and S_B are on, the voltage across L_g can be determined as

$$v_{L_g} = L_g \frac{di_g}{dt} = V_2 - v_g \quad (49)$$

where v_g is grid voltage.

When S_A and S_B are off, the inductor voltage is

$$v_{L_g} = L_g \frac{di_g}{dt} = -v_g \quad (50)$$

The slope of i_g during $S_{A,B}$ on-state ($\delta_{inv,ON}$) and off-state ($\delta_{inv,OFF}$) can be written as

$$\delta_{inv,ON} = \frac{di_g}{dt} = \frac{V_2 - v_g}{L_g}, \quad \delta_{inv,OFF} = \frac{di_g}{dt} = \frac{-v_g}{L_g} \quad (51)$$

Now one can predict the inductor current at the next sampling period ($i_g[k+1]$) from its current value ($i_g[k]$), by using the slopes already determined, i.e.

$$i_g[k+1] = i_g[k] + \delta_{inv,ON} t_{inv,ON} + \delta_{inv,OFF} t_{inv,OFF} \quad (52)$$

where $t_{inv,ON}$ and $t_{inv,OFF}$ are the $S_{A,B}$ on and off state dwell times, respectively.

The controller is intended to eliminate the error, i_e , between the reference current (i_g^*) and $i_g[k+1]$, which translates to

$$i_e = i_g^* - i_g[k+1] = i_g^* - i_g[k] - \delta_{inv,ON} t_{inv,ON} - \delta_{inv,OFF} t_{inv,OFF} = 0 \quad (53)$$

Then, $t_{inv,ON}$ and consequently the optimal modulation index can be determined as

$$m_{inv} = \frac{L_g (i_g^* - i_g[k]) + v_g[k] T_s}{V_2 T_s} \quad (54)$$

6 | EXPERIMENTAL VERIFICATION

To verify the analytical analysis and proper operation of the proposed EV converter, a laboratory hardware prototype shown in Figure 10 has been developed. The test conditions and the parameters of the proposed converter are reported in Table 4. The prototype consists of two stages, the proposed dc-dc converter and a conventional dc-ac converter. The control system of the proposed EV charger includes the control loop of the battery side current and the grid side current during both forward and backward directions. For both stages we have adopted two dead-beat control loops to regulate both battery side voltage and current in dc-dc stage and dc-link voltage and ac grid current in the dc-ac stage which are similar to the methods described in reference [25].

Figure 11 illustrates the steady-state step-up of the forward direction performance of the proposed bidirectional dc-dc converter under open loop operation mode and with output load of 162 W and duty cycle of 0.5736. It can be seen that the primary (secondary) side voltage is 40 V (180 V), the battery and load current is 4.05 A and 0.9 A, respectively.

Similarly, Figure 12 shows the performance of the converter in the backward direction and step-down mode under steady state operation and under the primary side current of 4.05 A.

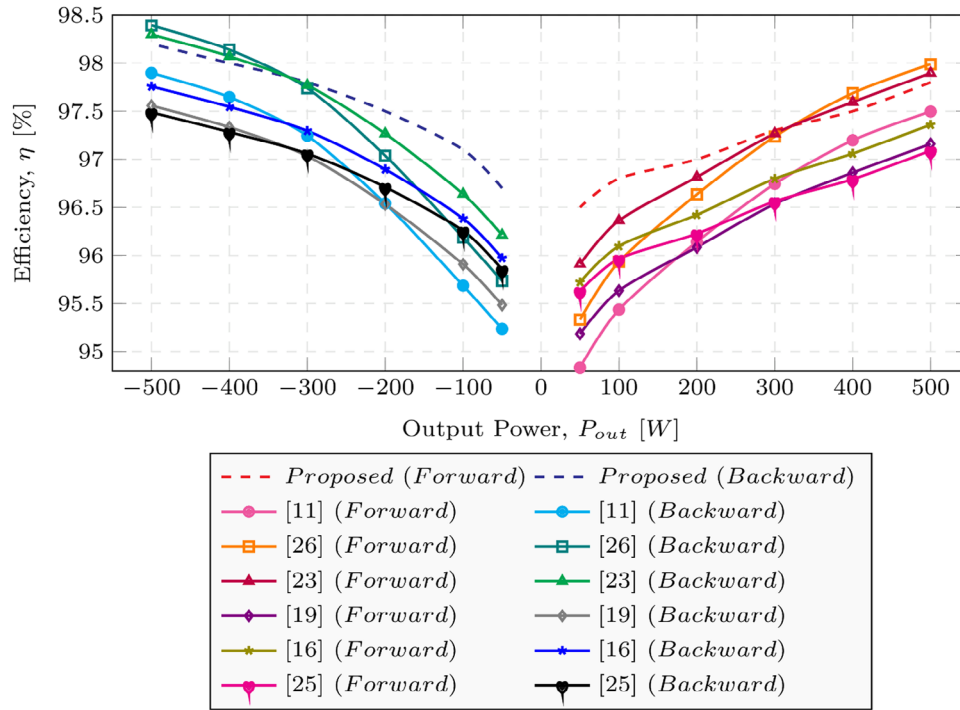


FIGURE 20 Bidirectional dc-dc converters calculated efficiency curve versus output power levels.

In this case, the input secondary side voltage is 180 V and since the battery is connected to the primary side, the output voltage is regulated to 40 V by the duty cycle of 0.4264.

The step-down operation mode at the forward direction and step-up mode at the backward direction is shown in Figure 13. In this figure, V_1 and V_2 is 200 V and 180 V, respectively. In the forward mode with respect to $D = 0.274$ and $i_2 = 0.9$ A, v_{C3} , i_{L1} , i_{L2} , and i_b is 275.7 V, 1.24 A, 1.71 A, and 0.81 A, respectively. Similarly, in the backward mode $D = 0.725$, $i_2 = 2.22$ A, $v_{C3} = 275.7$ V, $i_{L1} = 3.1$ A, $i_{L2} = 4.2$ A, and $i_b = 2$ A.

The DCM operation of the proposed bidirectional dc-dc converter during forward and backward direction modes are shown in Figures 14 and 15, respectively. The values of V_1 and V_2 with respect to D , D_1 and D_2 confirm the DCM voltage gains. In the DCM operation of forward direction mode, the duty cycle of switches is 0.2, while from Figure 14 D_1 and D_2 are 0.5769 and 0.6704, respectively. Therefore considering $V_1 = 40$ V, from (11) and (12) the voltages of C_3 and secondary side is 51.9 V and 29.9 V, respectively. Similarly, in the DCM operation of backward direction mode, D is 0.25, while from Figure 15 D_1 and D_2 are 0.16 and 0.5836, respectively. Considering $V_2 = 180$ V, from (23) and (24) the voltages of C_3 and primary side is 134.3 V and 40.28 V, respectively.

The steady state experimental results of the proposed bidirectional EV converter for the grid tied mode in terms of G2V and V2G operation is shown in Figure 16. The primary side current (or the battery current i_b) and the dc-link side voltage reference is 16 A and 180 V, respectively.

The measured outputs from the converter in response to a step change in the primary (battery) side current from 11 A to 16 A is shown in Figure 17(a and b) for V2G and G2V mode, respectively. As shown in this figure, the current of L_2 changes from 13.44 A to 19.55 A as the battery side current changes and the rms value of ac side current changes from 4 A to 5.64 A, while the primary and the secondary dc voltage level is fixed to 40 V and 180 V, respectively.

Furthermore, the output of the proposed bidirectional converter in response to a change from G2V (charging) to V2G (discharging) operation mode by a step change in current direction is shown in Figure 18. As illustrated in this figure, the primary (battery) side reference current changes from -16 A (charging) to $+16$ A (discharging), as a reaction of which, the current of L_2 changes from -19.55 to $+19.55$ A. In this test, a current rate limiter for i_{L2} is employed to ramp up the reference current.

The efficiency versus the output power curves for different direction modes are depicted in Figure 19. In the backward (charging or G2V) and forward (discharging or V2G) modes, the peak efficiencies of 97.6% and 97.2% are achieved, respectively.

Figure 20 displays the calculated efficiency for the proposed converter, as well as the converters from the references, all under identical conditions, i.e. same component parameters, voltages, and switching frequency. As shown in Figure 20, the proposed converter demonstrates a satisfactory level of efficiency when compared to other bidirectional dc-dc converters with identical parameters.

7 | CONCLUSION

The paper proposes a new bidirectional dc-dc converter for the EV charging system, capable of V2G and G2V application. The following conclusions can be stated:

1. The proposed dc-dc converter benefits from a boundless high voltage gain ratio in both directions, tolerable voltage and current stresses on MOSFET switches, a direct electrical connection between the input and output terminals, and having high energy transportation efficiency in both directions. The maximum efficiency of the proposed bidirectional dc-dc converter is 97.6% and 97.2% for charging and discharging mode, respectively at $V_1 = 40$ V, $V_2 = 180$ V, $P_{out} = 500$ W.
2. Although one published converter has higher voltage gain ratio, the proposed converter offers a wider range of the output voltage in both directions, while utilizing a lower number of switches.
3. The advantages of the proposed bidirectional dc-dc converter in terms of having a boundless, wide range and high voltage gain ratio make it a more practical and versatile EV charger compared to

AUTHOR CONTRIBUTIONS

Zahra Gholami: Development of the initial idea; methodology; data analysis; manuscript writing. **Rahim Ildarabadi:** Research design; development of the initial idea; data collection; data analysis; manuscript writing; review and editing; supervision. **Hamed Heydari-doostabad:** Development of the initial idea; methodology; research design; data collection; data analysis; manuscript writing. **Mohammad Monfared:** Research design; data analysis; manuscript writing; review and editing. **Terence O'Donnell:** Research design; data analysis; manuscript writing; review and editing; supervision.

ACKNOWLEDGEMENT

This work has been supported by Science Foundation Ireland under grant number SFI/21/SPP/3756.




CONFLICT OF INTEREST STATEMENT

The authors declare no conflicts of interest.

DATA AVAILABILITY STATEMENT

Data derived from public domain resources.

ORCID

Zahra Gholami  <https://orcid.org/0000-0002-6611-8058>
Rahim Ildarabadi  <https://orcid.org/0000-0002-5213-089X>
Mohammad Monfared  <https://orcid.org/0000-0002-8987-0883>

REFERENCES

1. Bose, B.K.: *Power Electronics in Renewable Energy Systems and Smart Grid*. Wiley-IEEE Press (2019)
2. Larminie, J., Lowry, J.: *Electric Vehicle Technology Explained*. Wiley & Sons Ltd (2012)
3. Ustun, T.S., Zayegh, A., Ozansoy, C.: Electric vehicle potential in Australia: Its impact on smart grids. *IEEE Ind. Electron. Mag.* 7(4), 15–25 (2013). <https://doi.org/10.1109/MIE.2013.2273947>
4. Seth, A.K., Singh, M.: Resonant controller of single-stage off-board EV charger in G2V and V2G modes. *IET Power Electronics* 13(5), 1086–1092 (2020). <https://doi.org/10.1049/iet-pel.2019.1111>
5. Bassa de los Mozos, A., Chandra Mouli, G.R., Bauer, P.: Evaluation of topologies for a solar powered bidirectional electric vehicle charger. *IET Power Electronics* 12(14), 3675–3687 (2019). <https://doi.org/10.1049/iet-pel.2018.5165>
6. Wang, Z., Wang, S.: Grid power peak shaving and valley filling using vehicle-to-grid systems. *IEEE Trans. Power Del.* 28(3), 1822–1829 (2013). <https://doi.org/10.1109/TPWRD.2013.2264497>
7. Johnson, P.: The Nissan LEAF is getting its first-ever V2G charger for selling energy back to the grid. (2022). [Online]. Available: <https://electrek.co/2022/09/07/the-nissan-leaf-getting-first-ever-v2g-charger/>
8. Safayatullah, M., Elrais, M.T., Ghosh, S., Rezaei, R., Batarseh, I.: A comprehensive review of power converter topologies and control methods for electric vehicle fast charging applications. *IEEE Access* 10(40), 40753–40793 (2022). <https://doi.org/10.1109/ACCESS.2022.3166935>
9. Do, H.-L.: Nonisolated bidirectional zero-voltage-switching DC-DC converter. *IEEE Trans. Power Electron.* 26(9), 2563–2569 (2011). <https://doi.org/10.1109/TPEL.2011.2111387>
10. Das, P., Laan, B., Mousavi, S.A., Moschopoulos, G.: A nonisolated bidirectional ZVS-PWM active clamped DC-DC converter. *IEEE Trans. Power Electron.* 24(2), 553–558 (2009). <https://doi.org/10.1109/TPEL.2008.2006897>
11. Caricchi, F., Crescimbeni, F., Di Napoli, A.: 20 kW water-cooled prototype of a buck-boost bidirectional DC-DC converter topology for electrical vehicle motor drives. In *Proceedings of 1995 IEEE Applied Power Electronics Conference and Exposition - APEC'95*, 2, 887–892 (1995). <https://doi.org/10.1109/APEC.1995.469045>
12. Lee, H.-S., Yun, J.-J.: High-efficiency bidirectional buck-boost converter for photovoltaic and energy storage systems in a smart grid. *IEEE Trans. Power Electron.* 34(5), 4316–4328 (2019). <https://doi.org/10.1109/TPEL.2018.2860059>
13. Khan, M.A., Husain, I., Sozer, Y.: A bidirectional dc-dc converter with overlapping input and output voltage ranges and vehicle to grid energy transfer capability. *IEEE J. Emerg. Sel. Top. Power Electron.* 2(3), 507–516 (2014). <https://doi.org/10.1109/JESTPE.2014.2305157>
14. Cortez, D.F., Waltrich, G., Fraigneaud, J., Miranda, H., Barbi, I.: Dc-dc converter for dual-voltage automotive systems based on bidirectional hybrid switched-capacitor architectures. *IEEE Trans. Ind. Electron.* 62(5), 3296–3304 (2015). <https://doi.org/10.1109/TIE.2014.2350454>
15. Chen, J., Sha, D., Yan, Y., Liu, B., Liao, X.: Cascaded high voltage conversion ratio bidirectional nonisolated DC-DC converter with variable switching frequency. *IEEE Trans. Power Electron.* 33(2), 1399–1409 (2018). <https://doi.org/10.1109/TPEL.2017.2679105>
16. Zhang, Y., Gao, Y., Zhou, L., Sumner, M.: A switched-capacitor bidirectional DC-DC converter with wide voltage gain range for electric vehicles with hybrid energy sources. *IEEE Trans. Power Electron.* 33(11), 9459–9469 (2018). <https://doi.org/10.1109/TPEL.2017.2788436>
17. Zhang, Y., Zhang, W., Gao, F., Gao, S., Rogers, D.J.: A switched-capacitor inter-leaved bidirectional converter with wide voltage-gain range for super capacitors in EVs. *IEEE Trans. Power Electron.* 35(2), 1536–1547 (2020). <https://doi.org/10.1109/TPEL.2019.2921585>
18. Elsayad, N., Moradisizkoobi, H., Mohammed, O.A.: Design and implementation of a new transformerless bidirectional dc-dc converter with wide conversion ratios. *IEEE Trans. Ind. Electron.* 66(9), 7067–7077 (2019). <https://doi.org/10.1109/TIE.2018.2878126>
19. Axelrod, B., Berkovich, Y., Beck, Y.: Family of universal bidirectional dc-dc converters with an extended voltage gain. *IET Power Electronics* 12(13), 3562–3570 (2019). <https://doi.org/10.1049/iet-pel.2018.6243>
20. Zhang, N., Zhang, G., See, K.W., Zhang, B.: A single-switch quadratic buck-boost converter with continuous input port current and continuous output port current. *IEEE Trans. Power Electron.* 33(5), 4157–4166 (2018). <https://doi.org/10.1109/TPEL.2017.2717462>

21. Rosas-Caro, J.C., Valdez-Resendiz, J.E., Mayo-Maldonado, J.C., Alejo-Reyes, A., Valderrabano-Gonzalez, A.: Quadratic buck-boost converter with positive out-put voltage and minimum ripple point design. *IET Power Electronics* 11(7), 1306–1313 (2018). <https://doi.org/10.1049/iet-pel.2017.0090>
22. Miao, S., Wang, F., Ma, X.: A new transformerless buck-boost converter with positive output voltage. *IEEE Trans. Ind. Electron.* 63(5), 2965–2975 (2016). <https://doi.org/10.1109/TIE.2016.2518118>
23. Heydari-doostabad, H., Hosseini, S.H., Ghazi, R., O'Donnell, T.: Pseudo dc-link EV home charger with a high semiconductor device utilization factor. *IEEE Trans. Ind. Electron.* 69(3), 2459–2469 (2022). <https://doi.org/10.1109/TIE.2021.3065623>
24. Zhang, Y., Gao, Y., Li, J., Sumner, M.: Interleaved switched-capacitor bidirectional dc-dc converter with wide voltage-gain range for energy storage systems. *IEEE Trans. Power Electron.* 33(5), 3852–3869 (2018). <https://doi.org/10.1109/TPEL.2017.2719402>
25. Heydari-doostabad, H., O'Donnell, T.: A wide range high voltage gain bidirectional dc-dc converter for V2G and G2V hybrid EV charger. *IEEE Trans. Ind. Electron.* 69(5), 4718–4729 (2022). <https://doi.org/10.1109/TIE.2021.3084181>
26. Hosseini, S.H., Ghazi, R., Heydari-Doostabad, H.: An extendable quadratic bidirectional dc-dc converter for V2G and G2V applications. *IEEE Trans. Ind. Electron.* 68(6), 4859–4869 (2021). <https://doi.org/10.1109/TIE.2020.2992967>
27. Pourmahdi, M., Heydari-doostabad, H., Ghazi, R., O'Donnell, T.: Buck-boost common ground bridgeless PFC (CGBPF) rectifies with positive/negative out- put. *IEEE Trans. Power Electron.* 37(2), 1272–1282 (2022). <https://doi.org/10.1109/TPEL.2021.3107364>
28. Aalami, M.R., Zarif, M., Alishahi, M., Shojaei, A.A., Doostabad, H.H.: Flying-inductor-cell based inverters for single-phase transformerless pv applications. *IET Power Electronics* 16(1), 75–91 (2023). <https://doi.org/10.1049/pel2.12364>
29. Heydari-doostabad, H., Pourmahdi, M., Jafarian, M., Keane, A., O'Donnell, T.: Three-switch common ground step-down and step-up single-stage grid-connected PV inverter. *IEEE Trans. Power Electron.* 37(7), 7577–7589 (2022). <https://doi.org/10.1109/TPEL.2022.3145193>
30. Truntic, M., Konjedic, T., Milanovic, M., Slibar, P., Rodic, M.: Control of integrated single-phase PFC charger for EVs. *IET Power Electronics* 11(11), 1804–1812 (2018). <https://doi.org/10.1049/iet-pel.2017.0663>
31. Abbaszadeh, M.A., Monfared, M., Heydari-doostabad, H.: High buck in buck and high boost in boost dual-mode inverter (Hb2DMI). *IEEE Trans. Ind. Electron.* 68(6), 4838–4847 (2021). <https://doi.org/10.1109/TIE.2020.2988240>
32. Pourfaraj, A., Monfared, M., Heydari-doostabad, H.: Single-phase dual-mode interleaved multilevel inverter for PV applications. *IEEE Trans. Ind. Electron.* 67(4), 2905–2915 (2020). <https://doi.org/10.1109/TIE.2019.2910041>
33. Heydari-doostabad, H., Monfared, M.: An integrated interleaved dual-mode time-sharing inverter for single-phase grid-tied applications. *IEEE Trans. Ind. Electron.* 66(1), 286–296 (2019). <https://doi.org/10.1109/TIE.2018.2829686>

How to cite this article: Gholami, Z., Ildarabadi, R., Heydari-Doostabad, H., Monfared, M., O'Donnell, T.: Bidirectional wide range and high voltage gain buck-boost DC-DC converter for EV chargers empowering V2G-G2V applications. *IET Power Electron.* 17, 230–250 (2024). <https://doi.org/10.1049/pel2.12630>